SN 2017hpa: A Nearby Carbon-rich Type Ia Supernova with a Large Velocity Gradient

Xiangyun Zeng[1,2] , Xiaofeng Wang[3,4] , Ali Esamdin[1] , Craig Pellegrino[5,6] , WeiKang Zheng[7] , Jujia Zhang[8,9,10] ,
Jun Mo[3], Wenxiong Li[3,11] , D. Andrew Howell[5,6], Alexei V. Filippenko[7,12] , Han Lin[3], Thomas G. Brink[7],
Edward A. Baron[13] , Jamison Burke[5,6] , James M. DerKacy[13] , Curtis McCully[5,6] , Daichi Hiramatsu[5,6] ,
Griffin Hosseinzadeh[5,14,15] , Benjamin T. Jeffers[7], Timothy W. Ross[7], Benjamin E. Stahl[7,16,21] , Samantha Stegman[7,17],
Stefano Valenti[18] , Lifan Wang[19], Danfeng Xiang[3], Jicheng Zhang[3], and Tianmeng Zhang[20]

[1] Xinjiang Astronomical Observatory, Chinese Academy of Sciences, Urumqi, Xinjiang 830011, People's Republic of China; aliyi@xao.ac.cn
[2] School of Astronomy and Space Science, University of Chinese Academy of Sciences, Beijing 100049, People's Republic of China
[3] Physics Department and Tsinghua Center for Astrophysics (THCA), Tsinghua University, Beijing, 100084, People's Republic of China
wang_xf@mail.tsinghua.edu.cn
[4] Beijing Planetarium, Beijing Academy of Science of Technology, Beijing 100044, People's Republic of China
[5] Department of Physics, University of California, Santa Barbara, CA 93106-9530, USA
[6] Las Cumbres Observatory, 6740 Cortona Drive Suite 102, Goleta, CA 93117-5575, USA
[7] Department of Astronomy, University of California, Berkeley, CA 94720-3411, USA
[8] Yunnan Observatories (YNAO), Chinese Academy of Sciences, Kunming 650216, People's Republic of China
[9] Key Laboratory for the Structure and Evolution of Celestial Objects, Chinese Academy of Sciences, Kunming 650216, People's Republic of China
[10] Center for Astronomical Mega-Science, Chinese Academy of Sciences, 20A Datun Road, Chaoyang District, Beijing, 100012, People's Republic of China
[11] The School of Physics and Astronomy, Tel Aviv University, Tel Aviv 69978, Israel
[12] Miller Senior Fellow, Miller Institute for Basic Research in Science, University of California, Berkeley, CA 94720, USA
[13] Homer L. Dodge Department of Physics and Astronomy, University of Oklahoma, USA
[14] Center for Astrophysics, Harvard & Smithsonian, 60 Garden Street, Cambridge, MA 02138-1516, USA
[15] Las Cumbres Observatory, 6740 Cortona Drive Suite 102, Goleta, CA 9311-5575, USA
[16] Department of Physics, University of California, Berkeley, CA 94720-7300, USA
[17] Department of Chemistry, University of Wisconsin, Madison, WI 53706, USA
[18] Department of Physics, University of California, Davis, CA 95616, USA
[19] George P. and Cynthia Woods Mitchell Institute for Fundamental Physics & Astronomy, Texas A&M University, Department of Physics and Astronomy, 4242
TAMU, College Station, TX 77843, USA
[20] Key Laboratory of Optical Astronomy, National Astronomical Observatories, Chinese Academy of Sciences, Beijing 100012, People's Republic of China

Abstract

We present extensive, well-sampled optical and ultraviolet photometry and optical spectra of the Type Ia supernova (SN Ia) 2017hpa. The light curves indicate that SN 2017hpa is a normal SN Ia with an absolute peak magnitude of $M_{max}^B \approx -19.12 \pm 0.11$ mag and a postpeak decline rate $\Delta m_{15}(B) = 1.02 \pm 0.07$ mag. According to the quasi-bolometric light curve, we derive a peak luminosity of 1.25×10^{43} erg s^{-1} and a ^{56}Ni mass of $0.63 \pm 0.02\,M_\odot$. The spectral evolution of SN 2017hpa is similar to that of normal Ia supernovae (SNe Ia), while it exhibits an unusually rapid velocity evolution resembling that of SN 1991bg-like SNe Ia or the high-velocity subclass of SNe Ia, with a postpeak velocity gradient of $\sim 130 \pm 7$ km s^{-1} day^{-1}. Moreover, its early spectra ($t < -7.9$ days) show a prominent C II $\lambda 6580$ absorption feature, which disappeared in near-maximum-light spectra but reemerged at phases from $t \sim +8.7$ days to $t \sim +11.7$ days after maximum light. This implies that some unburned carbon may mix deep into the inner layer and is supported by the low C II $\lambda 6580$-to-Si II $\lambda 6355$ velocity ratio (~ 0.81) observed in SN 2017hpa. The O I $\lambda 7774$ line shows a velocity distribution like that of carbon. The prominent carbon feature, the low velocity seen in carbon and oxygen, and the large velocity gradient make SN 2017hpa stand out from other normal SNe Ia and are more consistent with predictions from a violent merger of two white dwarfs. Detailed modeling is still needed to reveal the nature of SN 2017hpa.

Unified Astronomy Thesaurus concepts: Supernovae (1668); Type Ia supernovae (1728)

Supporting material: data behind figure, machine-readable table

1. Introduction

Type Ia supernovae (SNe Ia) are widely believed to arise from explosions of carbon–oxygen (CO) white dwarfs (WDs) in a binary system, which have a typical absolute V-band peak magnitude of ~ -19 mag (Phillips 1993; Perlmutter et al. 1999; Wang et al. 2006). The relatively uniform stellar explosions of SNe Ia make them useful as standardizable candles in measuring extragalactic distances (Phillips 1993; Riess et al. 1996; Guy et al. 2005; Wang et al. 2005; Howell 2011; Burns et al. 2018), leading to the discovery of the acceleration of the

universe (Riess et al. 1998; Perlmutter et al. 1999). In recent years, larger samples of SNe Ia have been used to further constrain the nature of dark energy driving the acceleration (e.g., Betoule et al. 2014; Abbott et al. 2019).

However, the progenitor systems and explosion mechanism of SNe Ia still remain controversial (e.g., Maoz et al. 2014). Two popular scenarios are the violent merger-triggered explosion of two WDs, known as the double-degenerate (DD) scenario (Iben & Tutukov 1984; Webbink 1984), and the accretion-triggered explosion of a WD with a nondegenerate companion, known as the single-degenerate (SD) scenario (Whelan & Iben 1973; Nomoto 1982; Nomoto et al. 1997). In general, the detection of signatures of circumstellar material

---

[21] Marc J. Staley Graduate Fellow.

(CSM) around some SNe Ia supports the SD scenario (Hamuy et al. 2003; Aldering et al. 2006; Patat et al. 2007; Sternberg et al. 2011; Dilday et al. 2012; Maguire et al. 2013; Silverman et al. 2013; Wang et al. 2019b), though some theoretical studies show that the CSM could be also produced in the DD scenario (Raskin & Kasen 2013; Shen et al. 2013). On the other hand, there is also evidence for nondetections of companion signatures for some SNe Ia, thus favoring the DD scenario (González Hernández et al. 2012; Schaefer & Pagnotta 2012; Olling et al. 2015; Tucker et al. 2019).

Popular explosion models of SNe Ia include the following cases. (1) The CO WD accretes material from the companion star until its mass nearly reaches the Chandrasekhar mass limit ($M_{\rm Ch} \sim 1.4\,M_{\odot}$, Chandrasekhar 1957) and compressional heating at the center causes the explosion (Piersanti et al. 2004). (2) The detonation of a thin layer of He on the surface of a WD (Kromer et al. 2010; Shen & Moore 2014) triggers a second detonation in the WD center and hence the explosion of a sub-$M_{\rm Ch}$ mass CO WD. (3) The violent merger or secular merger of two WDs occurs, accompanied by radiation of gravitational waves (Röpke et al. 2012; García-Berro & Lorén-Aguilar 2017). (4) In triple systems, oscillations of the third star cause a direct collision of two WDs and trigger the SN explosion (Thompson 2011; Mazzali et al. 2018). In view of these explosion mechanisms, the delayed-detonation model is one of the most suitable ones to account for the observed properties of SNe Ia; it initially involves a deflagration of a $M_{\rm Ch}$ CO WD and later a supersonic detonation (Khokhlov 1991; Höflich et al. 2017). Nevertheless, the double-detonation model of sub-$M_{\rm Ch}$ CO WDs shows many striking features and can also explain the observed properties of some SNe Ia (Shen et al. 2018).

Observationally, there is increasing evidence for spectroscopic and photometric diversity of SNe Ia. Most SNe Ia can be classified as spectroscopically normal ones, while a small fraction exhibit peculiar properties in some respects (e.g., Branch et al. 1993; Filippenko 1997), such as the SN 1991T-like overluminous SNe (Filippenko et al. 1992b; Ruiz-Lapuente et al. 1992; Phillips 1993), the SN 1991bg-like subluminous SNe (Filippenko et al. 1992a; Leibundgut et al. 1993), or the SN 2002cx-like subclasses (Filippenko 2003; Li et al. 2003). Based on differences in Si II velocity evolution, Benetti et al. (2005) divided SNe Ia into three subclasses: high velocity gradients (HVG), low velocity gradients (LVG), and FAINT (consists of faint SNe Ia). According to the equivalent width (EW) of the Si II $\lambda6355$ and Si II $\lambda5972$ absorption lines near maximum brightness, Branch et al. (2006) divided SNe Ia into core normal (CN), broad line (BL), cool (CL), and shallow silicon (SS) subgroups. The subluminous SN 1991bg-like and overluminous SN 1991T-like SNe Ia have large overlap with the CL and SS subclasses, respectively (Branch et al. 2006). Based on the Si II $\lambda6355$ velocity measured near the time of B-band maximum, Wang et al. (2009a) classified SNe Ia into normal-velocity (NV) and high-velocity (HV) subsets. The HV subclass is found to share some common properties, such as red $B - V$ color, slow decay in blue bands starting at $t \approx 40$ days from the peak, and abundant surrounding CSM (Wang et al. 2008, 2009b, 2019b; Foley et al. 2011; Mandel et al. 2014). Although asymmetric explosions have been proposed to explain the occurrence of HV and NV subclasses of SNe Ia (Maeda et al. 2010), it is difficult to account for the fact that

these two subgroups have different birth environments (Wang et al. 2013).

Early-time observations can place important constraints on the explosion physics of SNe Ia, including the size of the primary WD (Bloom et al. 2012), the radius of the companion star (Hosseinzadeh et al. 2017), the distribution of ^{56}Ni in the ejecta, and the possible existence of CSM (Piro & Morozova 2016). Therefore, clarifying the progenitor systems and explosion mechanisms affects our understanding of stellar evolution and precision cosmology. The unburned carbon detected in early-time spectra can provide important clues to the progenitor system and explosion mechanism of SNe Ia (Yamanaka et al. 2009; Silverman et al. 2011; Taubenberger et al. 2011; Thomas et al. 2011; Silverman & Filippenko 2012; Hsiao et al. 2013; Li et al. 2019).

Previous studies show that nearly 30% of SNe Ia show signatures of C II $\lambda6580$ absorption at $t \approx -4$ days (relative to the time of maximum light), while this fraction is over 40% when examining the $t \approx -10$ days spectra (Parrent et al. 2011; Thomas et al. 2011; Folatelli et al. 2012; Silverman & Filippenko 2012; Maguire et al. 2014). These studies show that carbon-positive SNe Ia tend to be LVG subtypes (Folatelli et al. 2012) and have bluer optical colors around maximum light (Thomas et al. 2011; Silverman & Filippenko 2012). Among those carbon-positive SNe Ia, two events show carbon absorption lasting until 1–3 weeks after maximum light. One is SN 2002fk, which has detectable carbon absorption lines in the $t \approx 10$ days spectrum (Cartier et al. 2014). Another example is SN 2018oh studied by Li et al. (2019), the first Kepler-discovered SN Ia with a spectroscopic classification; the carbon feature can be detected even in the $t \approx 20.5$ days spectrum, representing the latest detection of carbon in SNe Ia. The origin of these carbon detections in postmaximum spectra still remains unclear. SN 2017hpa is the third SN Ia with a persistent carbon feature; it exploded in the spiral galaxy UGC 3122 (see Figure 1) at a distance of $\sim$65.6 Mpc (redshift $z \approx 0.0156$). The prominent carbon features and small distance of SN 2017hpa provide us with another excellent chance to study the observed diversity of SNe Ia.

In this paper, the optical observations and data reduction are presented in Section 2. Section 3 discusses the light and color curves, while Section 4 shows the spectroscopic evolution. The quasi-bolometric light curve and the origin of the prominent carbon feature of SN 2017hpa are discussed in Section 5. We summarize in Section 6.

2. Observations and Data Reduction

2.1. Discovery and Host Galaxy

SN 2017hpa was discovered at $\alpha = 04^{\rm h}39^{\rm m}50^{\rm s}.750$, $\delta = 07°03'54''.90$ (J2000) on 2017 October 25.35 (UT dates are adopted throughout this paper) during the Puckett Observatory World Supernova Search (Gagliano et al. 2017). A spectrum taken $\sim$0.65 day after the discovery classified it as a normal SN Ia (Floers et al. 2017). Figure 1 shows a color image of SN 2017hpa synthesized from observations in gri bands.

The host galaxy of SN 2017hpa is UGC 3122, which is classified as SAB(rc)s at $z = 0.015631 \pm 0.000005$ (Springob et al. 2005). This redshift corresponds to a distance modulus $\mu = 34.05 \pm 0.38$ mag with a velocity uncertainty of
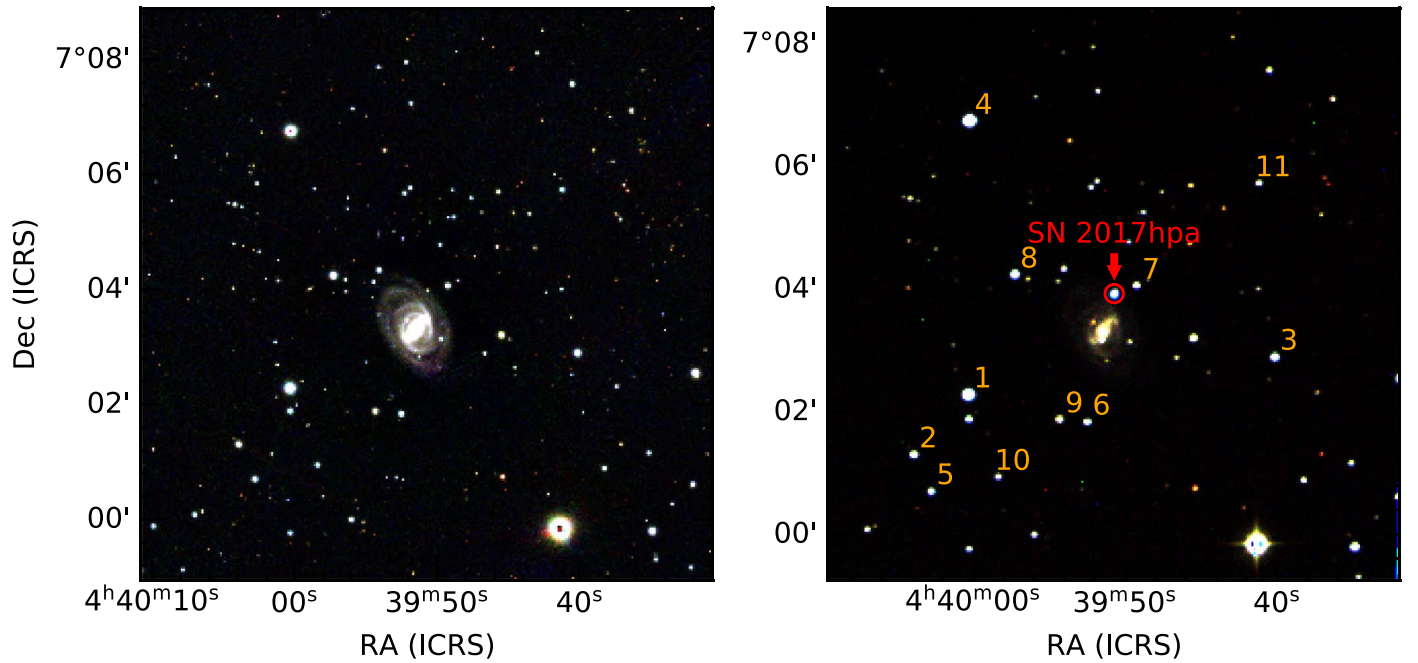
Figure 1. The left panel shows a color image synthesized from *gri*-band observations from PanSTARRS, and the faint star right beside the position of SN 2017hpa is totally covered in subsequent observations. The right panel shows a color image synthesized from *gri*-band observations from the Tsinghua-NAOC telescope; SN 2017hpa is marked with a red circle, while the reference stars are numbered.

$500 \, \mathrm{km \, s^{-1}}$ (Willick et al. 1997), assuming a Hubble constant of $73.5 \, \mathrm{km \, s^{-1} \, Mpc^{-1}}$ (Riess et al. 2018).

2.2. Photometry

After the discovery of SN 2017hpa, we triggered follow-up photometric observations on several telescopes, including the 0.8 m Tsinghua-NAOC telescope (TNT; Huang et al. 2012; Zhang et al. 2015), the Las Cumbres Observatory (LCO) Telescope network (Shporer et al. 2011; Brown et al. 2013), the 0.76 m Katzman Automatic Imaging Telescope (KAIT) at Lick Observatory (Filippenko et al. 2001; Li et al. 2001; Filippenko 2005), and the 1 m Nickel reflector at Lick Observatory. The TNT, Nickel, and KAIT monitored SN 2017hpa in the *BVRI* bands, while the LCO 1 m telescope sampled its light curves in the *BVgri* bands.

For photometric observations obtained from the LCO during the Global Supernova Project, PyZOGY (Zackay et al. 2016; Guevel & Hosseinzadeh 2017) is employed for image subtraction, while *lcogtsnpipe* (Valenti et al. 2016) is applied to measure the SN flux. An ad hoc pipeline (based on the IRAF DAOPHOT package; Stetson 1987) is applied to reduce images from the TNT and extract instrumental magnitudes of the SN. Photometric images from the Lick Observatory are reduced using the Lick Observatory Supernova Search (LOSS; Filippenko et al. 2001) data-reduction pipeline (Ganeshalingam et al. 2010; Stahl et al. 2019, 2020a), while DAOPHOT (Stetson 1987) is applied to implement the point-spread-function (PSF) photometry.

For the TNT instrumental magnitudes, the *BV*-band images are calibrated using the APASS catalog (Henden et al. 2016), and the *gri*-band magnitudes are calibrated using the PanSTARRS catalog (Chambers et al. 2016; Flewelling et al. 2020; Magnier et al. 2020; Waters et al. 2020). The local standard stars with photometric magnitudes from APASS and PanSTARRS are listed in Table 1. The unfiltered instrumental

magnitudes from LOSS are calibrated to the standard Landolt *R*-band magnitudes based on the transformed local standards of the Sloan Digital Sky Survey (Li et al. 2003; Zheng et al. 2017). The LOSS *BVRI* instrumental magnitudes are calibrated to the Johnson system using a series of Landolt (1992) standard stars taken on a number of photometric nights.

Optical and ultraviolet (UV) observations of SN 2017hpa were also obtained with the Neil Gehrels Swift Observatory (Gehrels et al. 2004). The Swift/UVOT observations started at relatively early phases in six bands including *uvw*2, *uvm*2, *uvw*1, *u*, *b*, and *v* (Roming et al. 2005). The filters in lowercase are used throughout this paper for photometric observations in UVOT bands. Using zero-points extracted by Breeveld et al. (2011) in the Vega system, we applied the data-reduction pipeline of the Swift Optical/Ultraviolet Supernova Archive (SOUSA; Brown et al. 2014) to obtain the Swift optical/UV light curves of SN 2017hpa. The source counts are measured using a $3''$ aperture, and corrections are based on the average PSF. The template-subtraction technique has also been applied to the Swift images, and the final uncertainty in the photometry is a combination of statistical uncertainties in galaxy subtraction count rates and a 2% systematic fluctuation at each pixel caused by differences in response sensitivity across the photon detector. The final observed Swift and ground-based light curves are shown in Figure 2, and the corresponding magnitudes are tabulated in Tables 2 and 3.

2.3. Spectroscopy

A total of 26 low-resolution optical spectra of SN 2017hpa have been obtained using different telescopes and equipment, including the AFOSC mounted on the Asiago Ekar telescope, the BFOSC mounted on the Xinglong 2.16 m telescope (XLT; Jiang et al. 1999; Fan et al. 2016; Zhang et al. 2016a), the YFOSC on the Lijiang 2.4 m telescope (LJT; Chen et al. 2001; Wang et al. 2019a) of Yunnan Astronomical Observatories, the

Table 1
Photometric Standards in the SN 2017hpa Field 1[a]

Star	α(J2000)	δ(J2000)	B (mag)	V (mag)	g (mag)	r (mag)	i (mag)
1	04:40:00.331	+07:02:17.167	14.125(020)	13.368(015)	13.689(014)	13.114(034)	12.915(040)
2	04:40:03.904	+07:01:18.451	16.618(065)	15.697(037)	16.160(089)	15.398(107)	15.110(070)
3	04:39:40.185	+07:02:54.100	15.836(029)	15.046(049)	15.403(030)	14.779(034)	14.593(045)
4	04:40:00.268	+07:06:44.968	14.140(034)	13.228(016)	13.625(016)	12.887(036)	12.632(035)
5	04:40:02.771	+07:00:42.491	16.812(121)	16.013(077)	16.389(088)	15.752(053)	15.491(174)
6	04:39:52.514	+07:01:50.567	17.515(169)	16.242(070)	16.645(040)	15.957(026)	15.637(040)
7	04:39:49.255	+07:04:03.612	17.125(095)	16.130(077)	16.594(044)	15.802(069)	15.477(068)
8	04:39:57.276	+07:04:14.560	15.626(052)	14.823(023)	15.191(018)	14.556(044)	14.326(043)
9	04:39:54.303	+07:01:52.794	17.553(151)	16.262(008)	16.918(114)	15.686(037)	15.101(034)
10	04:39:58.351	+07:00:56.540	17.480(238)	16.547(158)	16.996(066)	16.230(041)	15.995(040)
11	04:39:41.224	+07:05:43.976	17.430(026)	16.468(078)	17.033(093)	16.288(066)	16.102(040)

Note.
[a] Standard stars used for calibration of instrumental magnitudes.

Kast spectrograph on the Lick 3 m Shane telescope (Miller & Stone 1993; Stahl et al. 2020a), and the LCO 2 m Faulkes Telescope North (Brown et al. 2013). The journal of spectroscopic observations is presented in Table 4, including one spectrum from the Transient Name Server[22] and six spectra from Stahl et al. (2020a). When no data-reduction pipeline was available, we applied standard IRAF routines to reduce the spectra. Spectrophotometric standard stars observed at an air mass comparable to the target on the same night were used to calibrate the flux density of SN 2017hpa. The extinction curves of the various observatories are utilized to correct for atmospheric extinction, and spectra of the standard stars are used to eliminate the telluric absorption lines.

3. Light Curves

3.1. Optical and Ultraviolet Light Curves

The multiband UV/optical light curves of SN 2017hpa are shown in Figure 2; one can see that the observations in optical bands have nearly daily sampling, ranging from about 2 weeks before to over 100 days after B-band maximum light. The light curves of SN 2017hpa are similar to those of normal SNe Ia, reaching maximum slightly earlier in the I/i and UV bands than in the B band, and having a prominent shoulder in R/r as well as a secondary maximum in I/i. The slight deviations between the $BVgri$ light curves of different telescopes are primarily due to different filter transmission functions, as shown in Figure 3. The transmission differences at the red edge of the I-band filters may cause the I-band discrepancies between LCO and TNT. Applying a polynomial fit to the B-band light curves around maximum light yields a peak of 15.48 ± 0.03 mag on MJD $= 58066.6$ (UT 2017 November 9.6). The V-band light curve reached its peak of 15.35 ± 0.2 mag on MJD $= 58068.4$, $\sim$1.8 days after the B-band peak.

Figures 4 and 5 compare the multiband UV/optical light curves of SN 2017hpa with those of several well-observed normal SNe Ia that have comparable $\Delta m_{15}(B)$, including SN 2003du (Stanishev et al. 2007), SN 2005cf (Wang et al. 2009a), SN 2011fe (Maguire et al. 2013), SN 2012cg (Munari et al. 2013; Brown et al. 2014), SN 2013dy (Pan et al. 2015a; Zhai et al. 2016), and SN 2018oh (Li et al. 2019). The UV/optical light curves of the comparison SNe Ia have been normalized to SN 2017hpa. As can be seen from Figure 4, SN 2017hpa and

other normal comparison SNe Ia have similar light-curve shapes near B-band maximum. Although the UV light curves of SN 2017hpa are similar to those of other comparison SNe Ia, they seem to show excess emission at early phases, especially the first two data points. This may suggest additional energy beyond the radioactive decay of centrally located nickel, such as surface nickel mixing (Piro & Nakar 2013) or interaction of SN ejecta with a companion star or with CSM (Kasen 2010). The postpeak decline rate $\Delta m_{15}(B)$ of the B-band light curve is measured to be 1.02 ± 0.07 mag, and the color stretch (Burns et al. 2014) is determined to be $s_{BV} = 0.94 \pm 0.03$.

3.2. Reddening and Color Curves

Assuming $R_V = 3.1$ (Cardelli et al. 1989), we obtain the line-of-sight Galactic extinction for SN 2017hpa to be $A_V = 0.485$ mag (Schlegel et al. 1998; Schlafly & Finkbeiner 2011), corresponding to a color excess of $E(B - V)_{\rm gal} = 0.156$ mag. After removing the Galactic reddening, the $B - V$ color is found to be 0.002 ± 0.05 mag at $t = 0$ day and 1.08 ± 0.06 mag at $t = 35$ days relative to the B maximum, consistent with typical values of normal SNe Ia (Phillips et al. 1999; Wang et al. 2009a).

We applied SuperNovae in object-oriented Python (SNooPy; Burns et al. 2011, 2014) to fit the multiband light curves of SN 2017hpa, as shown in Figure 6. Both EBV and st models in SNooPy2 are adopted to estimate the host-galaxy extinction, and an average host reddening is derived to be $E(B - V)_{\rm host} = 0.06 \pm 0.06$ mag. The relatively low host-galaxy reddening is consistent with the fact that the SN is located far away from the center of the host galaxy. Moreover, the spectra of SN 2017hpa show no detectable absorption feature of Na I D that is due to the host galaxy.

The optical intrinsic color evolution of SN 2017hpa is shown in Figure 7. At $t \gtrsim -10$ days, both the $B - V$ and $g - r$ color curves evolve toward the red until reaching the reddest color at 4–5 weeks after the B maximum. Both the $V - I$ and $g - i$ color curves show a short-term evolution from red to blue until $t \approx -10$ days; then they evolve redward and reach the red peak at $t \approx 35$ days. After that, the $V - I$ and $g - i$ color curves became progressively bluer. Overall, the color-curve evolution of SN 2017hpa is similar to that of SN 2005cf and SN 2018oh, except it has a bluer color at very early phases (especially the $g - r$ color). Based on the near-UV (NUV) colors, SNe Ia can be classified into NUV-red and NUV-blue subgroups

---

[22] https://wis-tns.weizmann.ac.il/
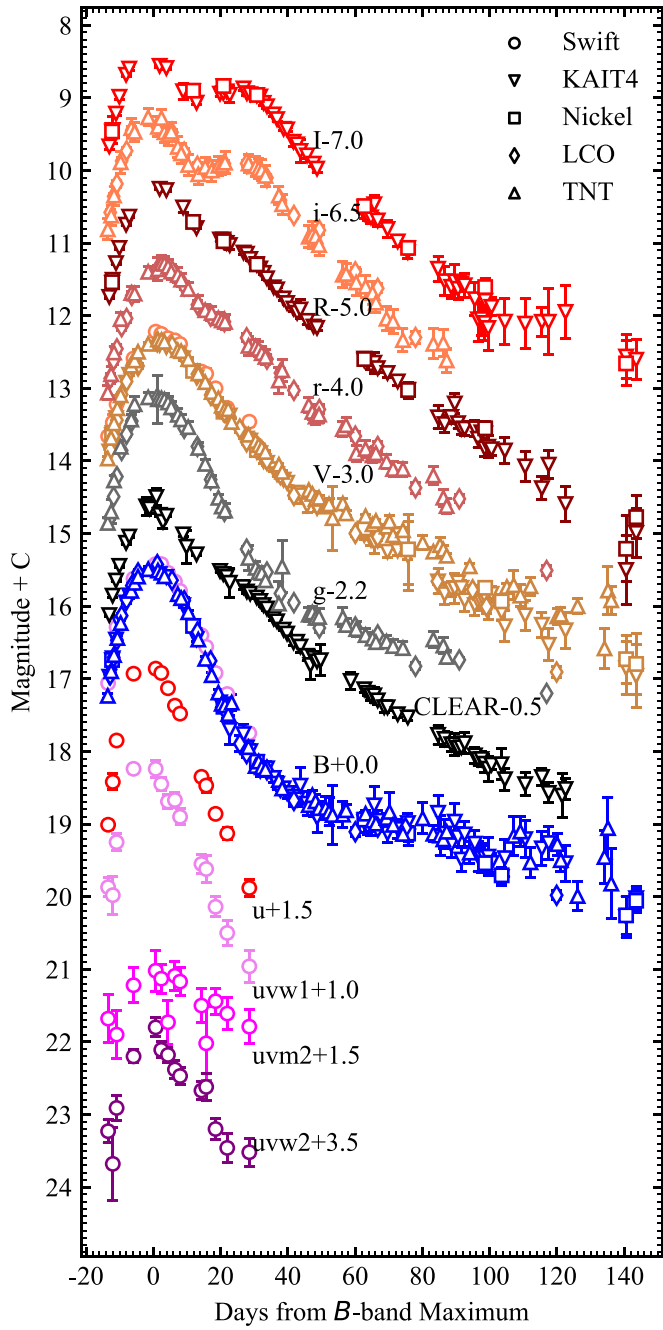
Figure 2. Observed UV and optical light curves of SN 2017hpa.

(Milne et al. 2013). Figure 8 shows the observed $uvw1 - V$ color evolution of SN 2017hpa together with that of SNe 2005cf, 2011fe, and 2018oh. One can see that SN 2017hpa can be put into the NUV-red group.

3.3. First-light Time

The rise time and first-light time can put additional constraints on the radius of the exploding star itself (Bloom et al. 2012; Piro & Nakar 2013). The observation on 2017 October 13 by Gagliano et al. (2017) provides a nondetection limit magnitude of 20.5 mag. However, this observation is about 12 days before the discovery and cannot provide a very useful constraint for the explosion date and hence the rise time of the light curves. We thus only utilized the discovery

magnitude, $17.9 \, \text{mag} \pm 0.3 \, \text{mag}$ in the clear band (close to broadband R), obtained at ~ 2.0 days before our multicolor observations when performing the rise-time fitting. The ideal expanding fireball (Riess et al. 1999) model and broken-power-law (Zheng & Filippenko 2017) model are both adopted to fit the R-band light curve of SN 2017hpa (as shown in Figure 9), and the first-light time of the light curve is estimated as 58047.08 ± 0.73 days and 58049.65 ± 0.24 days, respectively. The mean fitted first-light time (FFLT) is adopted as 58048.37 ± 0.97 days. With the time of maximum light in B and the derived FFLT, the rise time of SN 2017hpa is estimated to be 18.26 ± 0.97 days, comparable to that of typical SNe Ia (Zheng et al. 2017). The first multicolor observation of SN 2017hpa is thus estimated to be ~ 5 days after the FFLT, ~ 13 days prior to B maximum.

4. Optical Spectra

4.1. Temporal Evolution of the Spectra

The evolution of the optical spectra of SN 2017hpa is displayed in Figure 10. The early-time spectra are characterized by prominent absorption lines of intermediate-mass elements (IMEs), such as Fe II $\lambda\lambda$ 4404,5018, Mg II λ4481, Si II λ6355, S II $\lambda\lambda$ 5468,5654, Ca II NIR triplet, and Ca II H&K. At $t \sim 2$ weeks before the B-band maximum, the absorption troughs near 4300 Å and 4800 Å could be attributed to Fe II/Fe III/Mg II, while the distinct absorption notches near 6300 Å and 7000 Å could be due to C II λ6580 and C II λ7234, respectively. The C II λ6580 absorption is relatively strong, while the C II λ7234 absorption is weaker. The Si II λ6355 absorption lines at this phase display a perfect Gaussian profile without invoking the high-velocity feature (HVF), while a Ca II NIR HVF could be detected through multi-Gaussian fitting (Zhao et al. 2015, 2016). After $t \sim 1$ week before maximum light, both C II λ6580 and C II λ7234 absorptions are still prominent in the spectra of SN 2017hpa, and the absorption lines of "W"-shaped S II and Si II λ5972 start to emerge in the spectra of SN 2017hpa. With the decrease of the expansion velocity of the photosphere, the absorption minimum of the Si II λ6355 line gradually shifted redward, and the absorption lines of iron group elements and sulfur gradually increase in strength. At around the B-band maximum, the spectra are primarily dominated by "W"-shaped S II absorption features near 5400 Å and the blended absorption lines of Fe II and Si II/Si III near 4500 Å and Si II λ6355, while the C II features become invisible at this phase. By $t \sim 0$ day, the HVFs of the Ca II NIR triplet become relatively weak, and the photospheric component started to emerge in the spectra. At $t \sim +10$ days after the B maximum, the photospheric components of the Ca II NIR continue to gain strength and start to dominate the spectra features. Interestingly, the C II λ6580 absorption feature seems to reemerge in the spectra of SN 2017hpa around this phase, which is rarely seen in other SNe Ia. At about one month after the B-band maximum, the Ca II H&K lines and NIR triplet are the main spectral features. Meanwhile, the features of iron group elements begin to dominate in the spectra when the SN enters the early nebular phase. Figure 11 compares spectra of SN 2017hpa at several epochs with those of well-observed SNe Ia with similar $\Delta m_{15}(B)$.

For SN 2017hpa, the C II λ6580 and C II λ7234 absorptions appear stronger than those of the comparison SNe Ia in the early-phase spectra, as shown in Figure 11(a). Moreover, the

Table 2
Photometric Observations of SN 2017hpa by Ground-based Telescopes

MJD	Epoch[a]	B (mag)	V (mag)	R (mag)	I (mag)	g (mag)	r (mag)	i (mag)	Clear (mag)	Telescope
58053.34	−13.30	17.235(035)	16.967(022)	···	···	17.054(081)	17.060(097)	17.311(143)	···	TNT
58053.54	−13.10	16.971(031)	16.869(027)	16.741(023)	16.668(039)	···	···	···	16.623(022)	KAIT4
58053.82	−12.83	16.946(041)	16.848(030)	···	···	16.981(025)	16.863(065)	17.078(043)	···	LCO
58054.35	−12.29	16.897(033)	16.684(020)	···	···	16.896(167)	16.806(102)	17.122(136)	···	TNT
58054.36	−12.28	16.741(012)	16.634(008)	16.539(010)	16.463(015)	···	···	···	···	Nickel
58054.36	−12.28	16.744(012)	16.642(011)	16.546(011)	16.463(016)	···	···	···	···	KAIT4
58054.54	−12.11	16.717(027)	16.614(021)	16.505(019)	16.442(190)	···	···	···	16.355(024)	KAIT4
58054.84	−11.80	16.705(043)	16.659(042)	···	···	16.692(022)	16.614(058)	16.856(045)	···	LCO
58055.19	−11.45	16.674(031)	16.484(017)	···	···	16.469(074)	16.507(089)	16.846(130)	···	TNT
58055.54	−11.10	16.460(021)	16.409(017)	16.276(017)	16.217(030)	···	···	···	16.147(016)	KAIT4
⋮	⋮	⋮	⋮	⋮	⋮	⋮	⋮	⋮	⋮	⋮
58203.00	+136.35	19.821(478)	18.920(192)	···	···	···	···	···	···	TNT
58207.17	+140.52	20.258(264)	19.730(330)	20.210(455)	19.657(309)	···	···	···	···	Nickel
58207.17	+140.52	20.281(285)	19.851(363)	20.501(477)	19.562(302)	···	···	···	···	KAIT4
58210.16	+143.52	20.056(159)	19.796(416)	19.774(295)	···	···	···	···	···	Nickel
58210.16	+143.52	20.021(159)	19.960(435)	19.991(337)	19.606(277)	···	···	···	···	KAIT4

Note.
[a] Relative to the epoch of B-band maximum brightness (MJD = 58,066.6). Magnitudes are calibrated to the AB magnitude system.

(This table is available in its entirety in machine-readable form.)

Table 3
Swift UVOT Photometry of SN 2017hpa

MJD	Epoch[a]	$uvw2$ (mag)	$uvm2$ (mag)	$uvw1$ (mag)	u (mag)	b (mag)	v (mag)
58053.19	−13.45	19.73(16)	20.18(33)	18.87(13)	17.51(06)	17.06(04)	16.66(05)
58054.59	−12.06	20.18(50)	···	18.98(26)	16.92(11)	16.73(07)	16.47(11)
58055.71	−10.93	19.41(17)	20.40(33)	18.25(12)	16.35(05)	16.29(04)	16.22(06)
58060.76	−5.89	18.70(09)	19.72(24)	17.24(06)	15.43(03)	15.62(03)	15.59(04)
58067.35	0.70	18.30(13)	19.52(28)	17.24(12)	15.36(05)	15.42(04)	15.22(06)
58069.00	2.35	18.61(11)	19.63(20)	17.45(09)	15.42(03)	15.42(03)	15.25(04)
58071.00	4.34	18.68(10)	20.23(30)	17.69(10)	15.63(04)	15.54(03)	15.31(04)
58073.05	6.41	18.88(12)	19.59(20)	17.67(10)	15.87(04)	15.66(03)	15.34(04)
58074.59	7.95	18.97(12)	19.67(19)	17.90(11)	15.98(04)	15.79(03)	15.39(04)
58080.95	14.31	19.17(13)	20.00(24)	18.55(13)	16.85(06)	16.40(04)	15.77(04)
58082.35	15.71	19.12(19)	20.52(51)	18.62(18)	16.97(09)	16.56(05)	15.80(07)
58085.14	18.49	19.70(15)	19.94(18)	19.14(14)	17.36(06)	16.92(04)	16.00(04)
58088.60	21.96	19.96(20)	20.11(22)	19.50(17)	17.63(08)	17.21(05)	16.27(05)
58095.17	28.52	20.02(19)	20.29(23)	19.96(22)	18.38(12)	17.75(06)	16.46(06)

Note.
[a] Relative to the epoch of B-band maximum (MJD = 58,066.6). Magnitudes are calibrated to the Vega magnitude system.

O I λ7774 absorption line of SN 2017hpa seems to also be stronger than in the comparison SNe Ia, except for SN 2011fe and SN 2012cg. The pseudoequivalent width (pEW) of C II λ6580 is measured to be 14.0 ± 1.0 Å for SN 2017hpa at $t \approx -13$ days, while those measured for SNe 2005cf, 2011fe, and 2012cg are 8.0 ± 1.1 Å, 0.8 ± 0.2 Å, and 1.0 ± 0.6 Å, respectively. No C II absorption feature is detected in the spectra of SN 2013dy at similar phase. The corresponding pEW of O I λ7774 is measured as 52.0 ± 6.3 Å for SN 2017hpa at this epoch, comparable to that of SN 2011fe (48.2 ± 0.4 Å), while those measured for SNe 2012cg and 2013dy are 16.2 ± 1.4 Å and 16.3 ± 3.4 Å, respectively. No prominent O I λ7774 is detected in the spectra of SN 2005cf at similar epoch, which is consistent with the findings by Wang et al. (2009b). Later, Zhao et al. (2016) discovered that the velocity of the O I λ7774 line shows a positive correlation with that of C II λ6580. We propose that more unburned carbon and oxygen may be kept in the explosion ejecta of SNe 2017hpa, 2011fe, and 2012cg, although the stronger O I λ7774 absorption

observed in SN 2017hpa could result from the higher oxygen abundance of the exploding white dwarf (Cui et al. 2020). A detached Ca II NIR HVF could be detected through multi-Gaussian fitting as proposed by Zhao et al. (2015, 2016).

Figure 11(b) shows the comparison at ∼1 week before maximum light. All spectra show an increase in absorption strength of IMEs. The Si II λ6355 velocity of SN 2017hpa derived from the absorption minimum is $12,500 \pm 180$ km s^{-1}, which is comparable to that of the comparison sample. The C II λ6580 absorption line remained visible in the red wing of Si II λ6355 at this epoch.

The spectra near maximum light are displayed in Figure 11(c). The absorption features due to IMEs such as Si II at 4130 Å, Si III at 4560 Å, and S II at 5468, 5612, and 5654 Å become prominent at this phase. The C II absorption features at around 6300 and 7000 Å remain noticeable in SN 2017hpa, but they are barely seen in the comparison SNe Ia. The R(Si II), defined as the line-strength ratio of Si II λ5972 to Si II λ6355 (Nugent et al. 1995), can be used as an indicator of
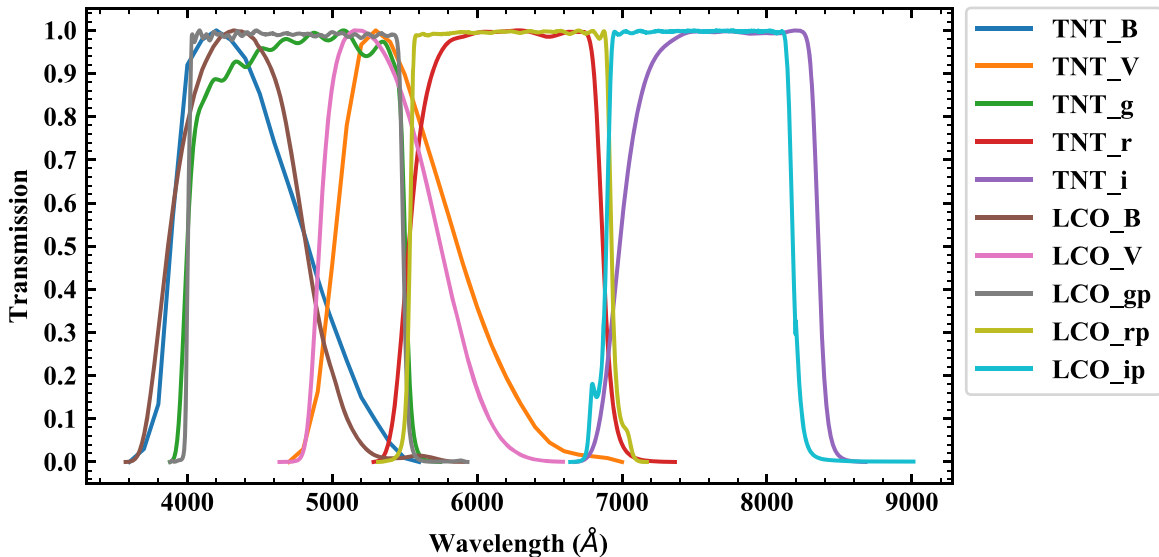
Figure 3. Transmission curves of the TNT and LCO filters; each curve is normalized to the peak.

Table 4
Spectroscopic Observations of SN 2017hpa

MJD	Epoch[a]	λ_{Start}	λ_{End}	Instrument
58052.5	−14.1	3387	8249	Asiago (public)
58053.2	−13.5	3496	9173	LJT
58054.2	−12.4	3502	9171	LJT
58056.5	−10.1	3622	10400	Lick 3 m
58058.7	−7.9	3399	9999	LCO
58064.5	−2.1	3249	9999	LCO
58068.7	2.0	3249	9999	LCO
58071.3	4.7	3746	8840	XLT
58075.4	8.7	3250	10000	LCO
58076.1	9.5	3744	8839	XLT
58078.4	11.7	3630	10400	Lick 3 m
58091.7	25.1	3500	9100	LJT
58094.3	27.7	3299	9999	LCO
58099.3	32.6	3299	9999	LCO
58099.3	32.6	3630	10400	Lick 3 m
58105.4	38.7	3632	10400	Lick 3 m
58107.7	41.1	3500	9100	LJT
58110.3	43.7	5896	8182	Lick 3 m
58111.3	44.7	3249	10000	LCO
58118.7	52.1	3500	9100	LJT
58119.4	52.8	3300	10000	LCO
58121.3	54.7	3299	10000	LCO
58127.8	61.1	3500	9100	LJT
58131.4	64.7	3632	10400	Lick 3 m
58132.3	65.7	3400	9300	LCO
58153.3	86.6	3300	9299	LCO

Note.
[a] Relative to the epoch of B-band maximum (MJD = 58,066.6).

the photospheric temperature. A lower value of $R(\mathrm{Si\,II})$ corresponds to a higher photospheric temperature for the SNe Ia. At around maximum light, $R(\mathrm{Si\,II})$ is measured to be 0.18 ± 0.03, comparable to that of SN 2018oh ($R(\mathrm{Si\,II}) = 0.15 \pm 0.04$), suggesting that these two SNe have similar photospheric temperatures around maximum light. The relatively larger ratio indicates a lower photospheric temperature for SN 2017hpa. The pEWs of Si II $\lambda5972$ and Si II $\lambda6355$ near maximum light are measured to be 15.5 ± 0.6 Å and

83.9 ± 2.2 Å, respectively, putting SN 2017hpa into the CN subtype of the Branch et al. (2006) classification.

Figure 11(d) shows the spectral evolution at $t \approx 30$ days. The C II $\lambda6580$ absorption line disappeared in this phase in all of our objects. With the receding of the photosphere, the Fe II features gain strength and gradually dominate at wavelengths between 4700 and 5000 Å. The absorption profiles of SN 2017hpa and the comparison sample are well developed and tend to have uniform morphologies.

4.2. Carbon Features

The presence of C II absorption can be easily identified in the early-time spectra of SN 2017hpa around 6300 and 7000 Å. The C II absorption features of SN 2017hpa are stronger than in the comparison SNe Ia. The left panel of Figure 12 shows that the C II $\lambda6580$ absorption lines persist in the spectra from $t \approx -14.1$ to -7.9 days. This absorption feature disappeared in the spectra approaching maximum light and then reemerged at $t \approx 9.5$ days. As a possible explanation, we propose that the C II will be highly excited when the detonation front or the deflagration front propagates outward through the ejecta of SNe Ia (Ciaraldi-Schoolmann et al. 2013; Seitenzahl et al. 2013), and this will make the C II absorption features disappear temporarily. With the receding and cooling of the photosphere of SNe Ia, the C II absorption trough will reemerge in the spectra. The right panel of Figure 12 shows the relatively weak C II $\lambda7234$ absorption; it is noticeable in the earliest four spectra, and it then became flattened. Inspection of the spectra does not reveal significant absorption of C II $\lambda4267$ in SN 2017hpa. Both C II $\lambda6580$ and C II $\lambda7234$ became barely visible in the spectra taken ~10 days after maximum light.

The SN Spectroscopic Evolution[23] package is employed to fit the absorption components of Si II $\lambda6355$ and C II $\lambda6580$. For SN 2017hpa, the C II $\lambda6580$ velocity is found to range from ~13,000 km s^{-1} at $t \approx -14.1$ days to ~9300 km s^{-1} at $t \approx -7.9$ days. According to Silverman & Filippenko (2012), the average velocity ratio between C II $\lambda6580$ and Si II $\lambda6355$ is ~1.05 for SNe Ia with observations at least four days prior to

---

[23] https://mwvg-spec-evolve.readthedocs.io/en/latest/
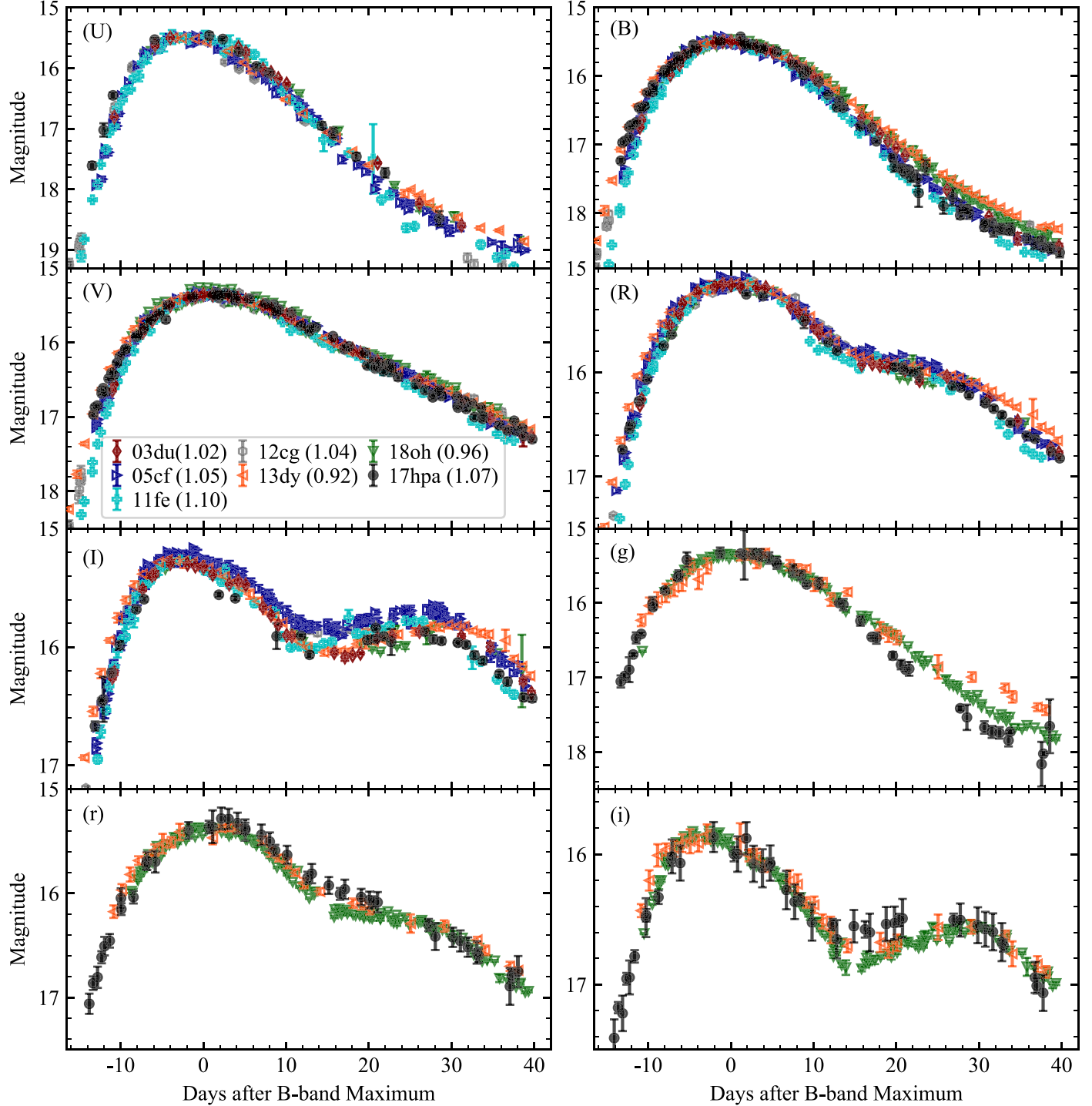
Figure 4. Comparison of the optical light curves of SN 2017hpa with other well-observed SNe Ia having similar decline rates. The light curves of the comparison SNe Ia have been normalized to match the observed peak magnitudes of SN 2017hpa.

B-band maximum light. However, the mean C II $\lambda6580$-to-Si II $\lambda6355$ velocity ratio (hereafter R(C II/Si II)) measured for SN 2017hpa is only ~0.81 (as shown in Figure 13), suggesting that significant unburned carbon may have mixed deep into the ejecta.

4.3. Ejecta Velocity

The ejecta velocities measured from the absorption lines, such as S II $\lambda\lambda$ 5468,5640, Si II $\lambda6355$, C II $\lambda6580$, C II $\lambda7234$,

and O I $\lambda7774$, are shown in Figure 14. The photospheric velocity measured from Si II $\lambda6355$ at $t \approx -13.5$ days is ~16,000 km s^{-1}, which is comparable to that of the Ca II NIR triplet (~16,200 km s^{-1}), but it is faster than the C II velocity (~12,000 km s^{-1} for both C II $\lambda6580$ and C II $\lambda7234$). The velocity of the C II $\lambda6580$ absorption is roughly within the typical expansion velocity of normal SNe Ia (Silverman & Filippenko 2012). At the time of *B*-band maximum, the velocity of Si II $\lambda6355$ is estimated to be ~9550 ± 170 km s^{-1}, which can put SN 2017hpa into the NV subclass in the
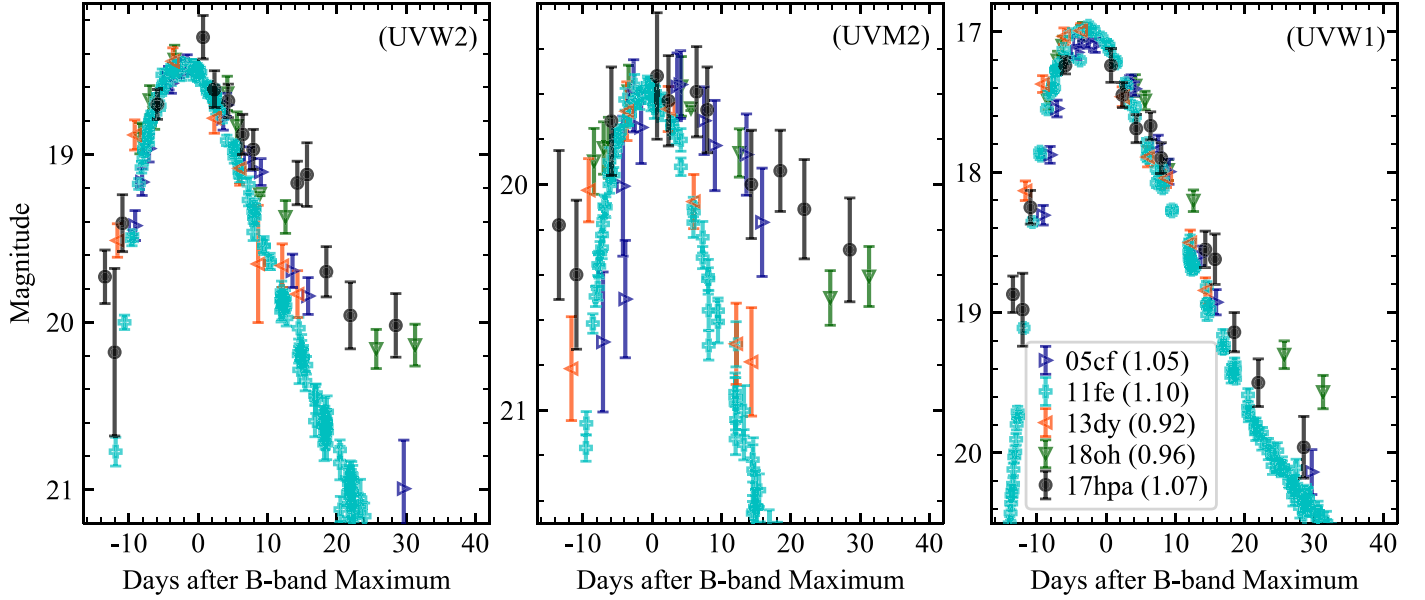
Figure 5. Comparison of the UV light curves of SN 2017hpa with other well-observed SNe Ia having similar decline rates. The light curves of the comparison SNe Ia have been normalized to match the peak magnitudes of SN 2017hpa.
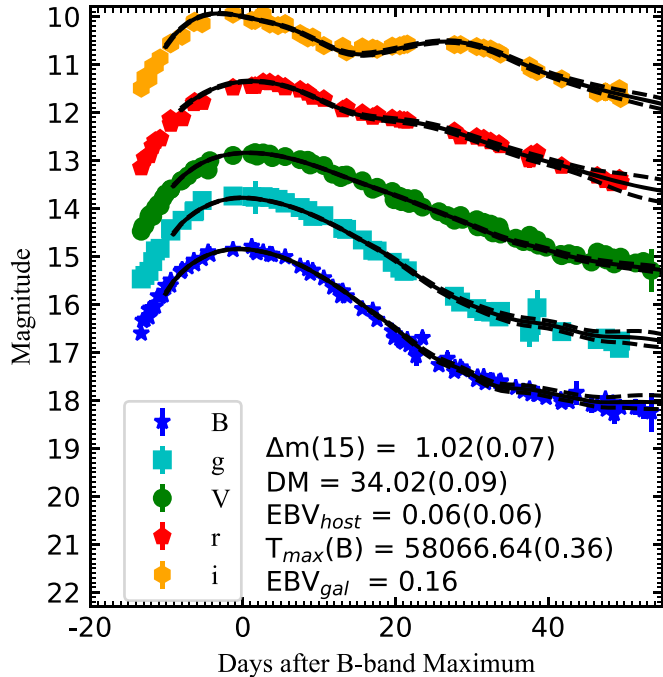
Figure 6. Best-fit light-curve model from SNooPy2. The light curves are shifted vertically for clarity. The dashed lines represent the 1σ uncertainty of the best-fit light-curve templates.

Wang et al. (2009a) classification scheme (the basic parameters of SN 2017hpa are listed in Table 5), as shown in Figure 15. However, the Si II $\lambda6355$ velocity of SN 2017hpa seems to have a large gradient, $\sim130 \pm 7$ km s^{-1} day^{-1}, measured within about 10 days after maximum light.

4.4. High-velocity Feature

At early phases, the HVFs of the Ca II NIR triplet can be clearly recognized from the corresponding absorption-line profiles in the spectra. We utilize a multi-Gaussian function to fit the absorption profile of the Ca II NIR triplet following the method described by Zhao et al. (2015, 2016). For SN 2017hpa, the HVF of the Ca II NIR triplet seen in the $t \approx -13.5$ days spectrum has a velocity of $\sim24,000$ km s^{-1}, comparable to that of SN 2011fe ($\sim22,000$ km s^{-1}; Zhang et al. 2016b). The Ca II NIR HVFs exhibit a velocity plateau of 20,000 km s^{-1} from $t \approx -10$ to -2 days, which is similarly seen in SN 2018oh but at different epochs (Li et al. 2019). Note that there are no obvious Si II HVFs in the early-phase spectra of SN 2017hpa. It is suggested that HVFs are more commonly detected in line profiles of the Ca II NIR triplet than in Si II (Maguire et al. 2012, 2014; Childress et al. 2014; Pan et al. 2015b; Silverman et al. 2015). Most SNe Ia are found to have strong Ca II NIR HVFs in their spectra at $t < 7$ days, while no more than 30% of them have strong Si II HVFs (Zhao et al. 2015).

5. Discussion

5.1. Distance and Quasi-bolometric Light Curve

Applying a standard cosmological model and assuming $H_0 = 73.5$ km s^{-1} Mpc^{-1}, $\Omega_M = 0.3$, and $\Omega_\Lambda = 0.7$ (Riess et al. 2018), we can obtain a distance modulus of ~34.05 mag for the host galaxy of SN 2017hpa. We also utilize the latest *EBV* model of SNooPy2 to fit the light curves of SN 2017hpa in several optical bands, and the best-fit result gives an average distance modulus of 34.00 ± 0.09 mag. These two distance moduli agree well with each other within the uncertainties. Adopting the distance modulus as 34.00 ± 0.09 mag and assuming $R_V = 3.1$, we derive the absolute *B*-band peak magnitude to be $M_{max}(B) = -19.12 \pm 0.11$ mag after correcting for both Galactic and host-galaxy extinction. This value agrees well with the typical value of normal SNe Ia ($M_{max}(B) \approx -19.3$ mag; Phillips et al. 1999; Wang et al. 2009a).

Our extensive photometric observations are used to establish the quasi-bolometric light curve of SN 2017hpa. The spectral energy distribution (SED) includes flux contributions from the
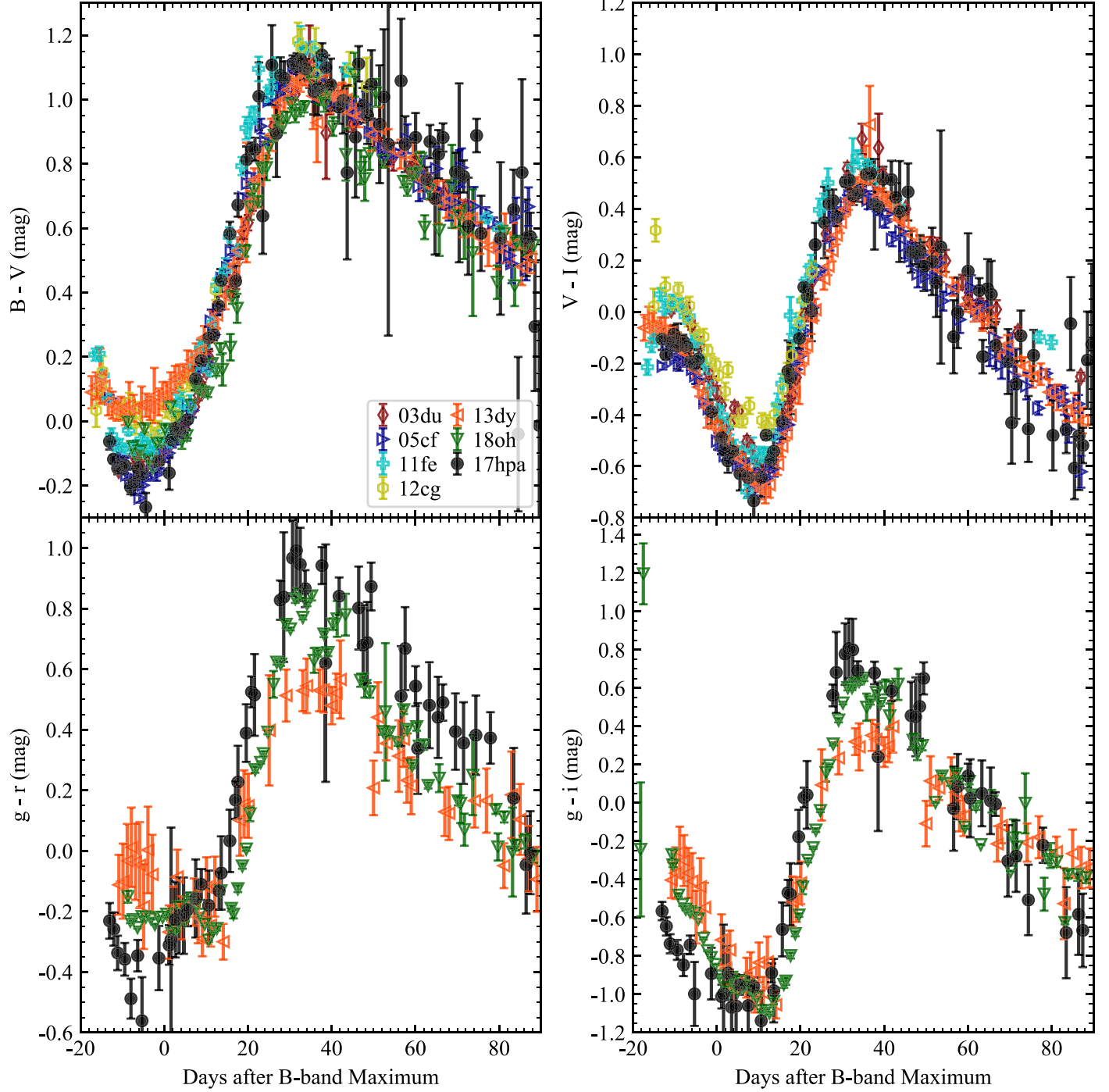
Figure 7. The $B - V$, $V - I$, $g - r$, and $g - i$ color curves of SN 2017hpa compared with those of SNe 2003du, 2005cf, 2011fe, 2012cg, 2013dy, and 2018oh. All light curves including those of SN 2017hpa have been dereddened using SNooPy2.

following bands: $uvw2$, $uvm2$, $uvw1$, B, g, V, R, r, I, and i. We adopt the procedure used for SN 2018oh to establish the SED at several epochs (Li et al. 2019). The observed magnitudes are dereddened and converted into flux density. The flux densities are then integrated using Simpson's rule (Rogers 1920; Syam 2003) through the effective wavelengths.

To get better knowledge of the peak luminosity, we use the UV and optical observations to construct the quasi-bolometric light curves by assuming the NIR contribution to be 5% at maximum light (Leloudas et al. 2009; Wang et al. 2009b; Zhai et al. 2016; Zhang et al. 2016b). Applying a polynomial fitting,

we estimate the maximum luminosity to be $L_{\mathrm{peak}} = 1.25 \times 10^{43}$ erg s^{-1} at about 0.85 day prior to B-band maximum. This peak luminosity is comparable to that of SN 2011fe ($\sim 1.13 \times 10^{43}$ erg s^{-1}; Zhang et al. 2016b) but lower than that of SN 2018oh ($\sim 1.49 \times 10^{43}$ erg s^{-1}; Li et al. 2019).

The modified radiation diffusion model of Arnett (Arnett 1982; Chatzopoulos et al. 2012; Li et al. 2019) is applied to evaluate the initial nickel mass together with other physical parameters of the SN ejecta. The Minim Code (Chatzopoulos et al. 2013) is used to fit the quasi-bolometric light curve with a constant opacity approximation. The model
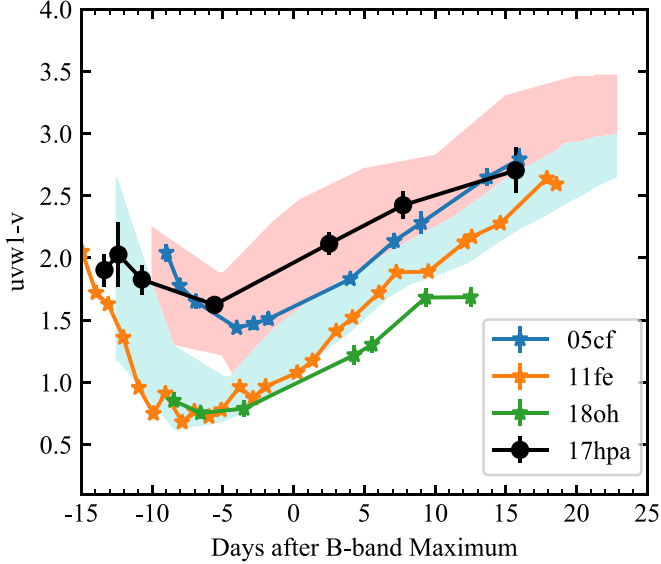
Figure 8. The $uvw1 - v$ color of SN 2017hpa compared to the group of NUV-blue and NUV-red SNe. The pink shaded region represents the regions covered by SNe Ia that are classified as NUV-red, and the blue shaded region represents the regions covered by SNe Ia that are classified as NUV-blue. The overplotted curve is the unreddened color evolution of SN 2017hpa (see Milne et al. 2013).
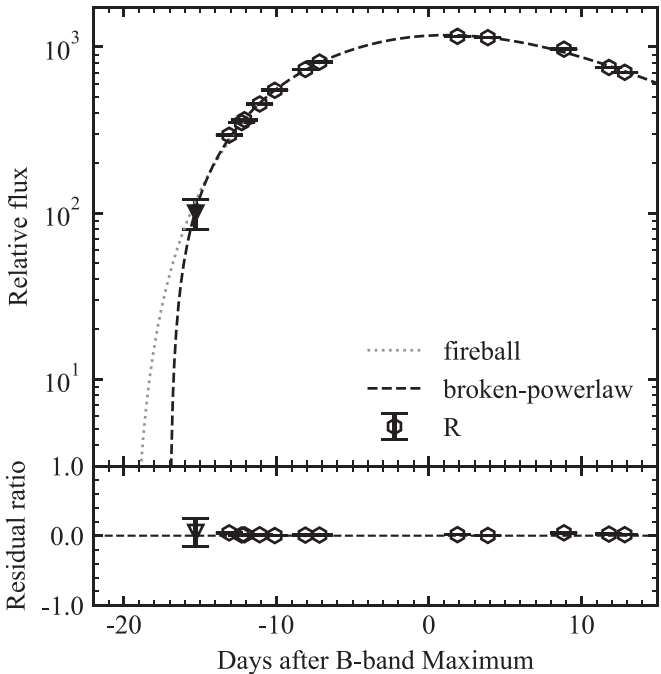
Figure 9. Fit to the observed R-band light curves using the analytic function from Zheng & Filippenko (2017) and the ideal fireball model (Riess et al. 1999). The black triangle represents the discovery magnitude, 17.9 mag $\pm$ 0.3 mag in the clear band (close to broadband R), obtained at $\sim$2.0 days before our multicolor observations. The bottom panel shows the residual relative to the best-fit curves. The horizontal dashed line in the bottom panel represents zero residual.

input parameters are the first-light time (FLT) t_0, the radioactive ^{56}Ni ejecta mass $M_{\rm Ni}$, the timescale $t_{\rm lc}$ of the light curve, and the leaking timescale of gamma rays t_γ (see, e.g., Chatzopoulos et al. 2012, 2013). We set all of these parameters free when performing the model fitting. The final best-fit result of the quasi-bolometric luminosity evolution of SN 2017hpa is shown
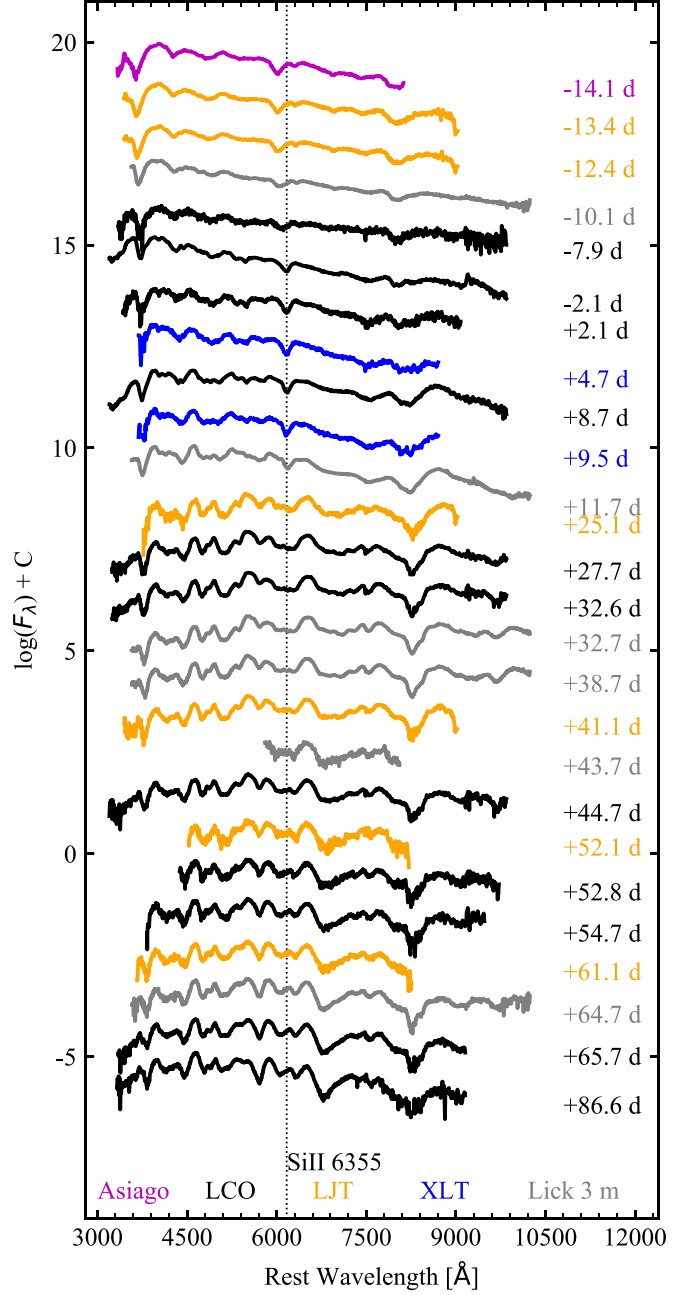
Figure 10. Optical spectral evolution of SN 2017hpa. All of the spectra have been corrected for the redshift of the host galaxy and reddening. The epochs shown on the right side represent the phases in days relative to B-band maximum light. The dashed line marks the center of the Si II λ6355 line profile at +2.04 days from the B-band maximum. The color of the spectrum stands for different instruments. The spectra have been shifted vertically for clarity.

(The data used to create this figure are available.)

in Figure 16. Based on χ^2 minimization, a set of parameters is found: $t_0 = -0.94 \pm 1.06$ days, $t_{\rm lc} = 15.86 \pm 0.76$ days, $M_{\rm Ni} = 0.63 \pm 0.02 \, M_\odot$, and $t_\gamma = 28.37 \pm 3.44$ days. The initial nickel mass is comparable to the estimates of $M_{\rm Ni} \approx 0.57 \, M_\odot$ for SN 2011fe (Zhang et al. 2016b) and $0.55 \pm 0.04 \, M_\odot$ for SN 2018oh (Li et al. 2019), but smaller than that of $0.77 \pm 0.11 \, M_\odot$ for SN 2005cf (Wang et al. 2009b) and $0.68 \pm 0.14 \, M_\odot$ for SN 2003du (Stanishev et al. 2007).
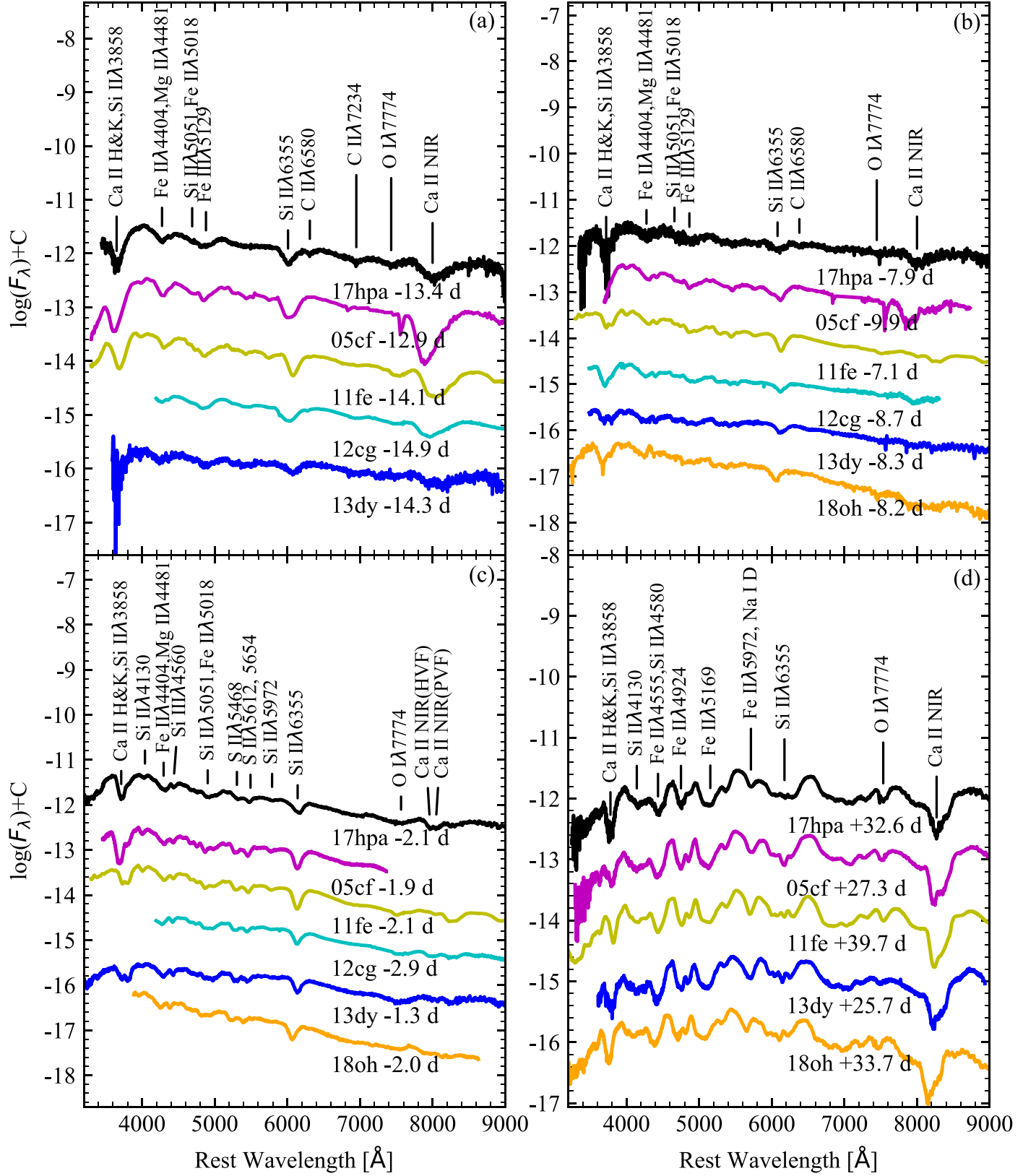
Figure 11. Spectra of SN 2017hpa at $t \approx -14$, -8, -2, and $+32$ days relative to B-band maximum, compared with spectra of SNe 2005cf (Garavini et al. 2007; Wang et al. 2009b), 2011fe (Mazzali et al. 2014; Zhang et al. 2016b), and 2013dy (Zheng et al. 2013; Pan et al. 2015a; Zhai et al. 2016) at comparable phases. Correction of reddening and redshift of the host galaxy had been done for all of the given spectra. The spectra have been shifted vertically for clarity.

Adopting the method used by Li et al. (2019), we estimate the average opacity κ to be 0.36 ± 0.15 cm^2 g^{-1}. With the best-fit $t_{\rm lc}$ and t_{γ}, we then obtain the ejecta mass and kinetic energy

as $M_{\rm ej} = 0.70 \pm 0.22 \, M_{\odot}$ and $E_{\rm kin} = (0.70 \pm 0.50) \times 10^{51}$ erg. These values are within the range of typical SNe Ia as suggested by Scalzo et al. (2019).
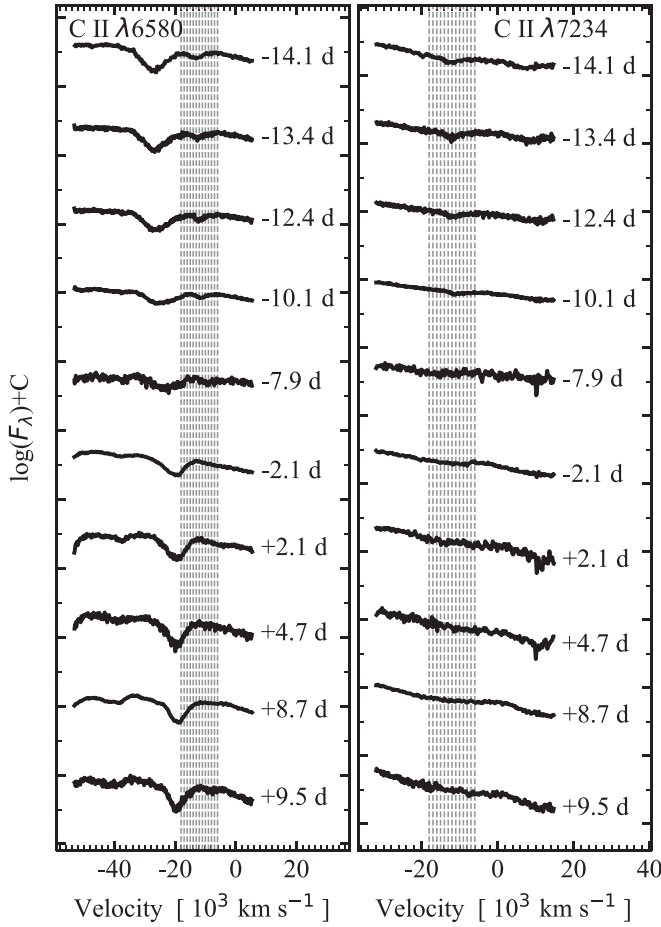
Figure 12. The left panel shows the C II λ6580 temporal evolution, while the right panel shows that of C II λ7234. The dashed lines mark the Doppler velocity range from −18,000 to −5000 km s⁻¹.

Figure 13. Top panel: temporal evolution of the C II λ expansion velocity for SNe Ia with carbon detections. Bottom panel: temporal evolution of the velocity ratio of C II λ6580 to Si II λ6355. The comparison data are taken from Silverman & Filippenko (2012).

5.2. High Velocity Gradient

The ejecta velocity (i.e., $9550 \pm 170 \, \text{km s}^{-1}$) measured for SN 2017hpa near maximum light is comparable to that of normal SNe Ia. According to the velocity gradient of the Si II, SNe Ia can be divided into LVG, HVG, and FAINT subtypes (Benetti et al. 2005). Most normal-velocity (as opposed to HV) SNe Ia tend to be LVG or FAINT objects (Silverman et al. 2012b). The left panel of Figure 17 shows the scatter plot of the $\Delta m_{15}(B)$ versus velocity gradient of SNe Ia, and the right panel displays that of the velocity gradient versus velocity measured around the time of maximum light. It can be seen that SN 2017hpa should be classified in the HVG subcategory, contradicting the trend that SNe Ia showing prominent carbon features tend to be LVG objects (Parrent et al. 2011). According to previous studies, HV SNe Ia tend to have larger velocity gradients and vice versa, while this tendency seems to be broken by SN 2017hpa.

Previous studies have shown that for the HVG and LVG subclasses, the difference in velocity gradient may be due to the different nature of the explosion or the mixing degree of heavy elements (Sahu et al. 2013). An off-center ignition will trigger SNe to explode asymmetrically. In this case, different viewing angles will cause the observed velocity gradient to vary greatly (Maeda et al. 2010). It is suggested that varying the criterion for the deflagration-to-detonation transition (DDT; Woosley et al. 2009) in explosions also can result in a wide range of velocity
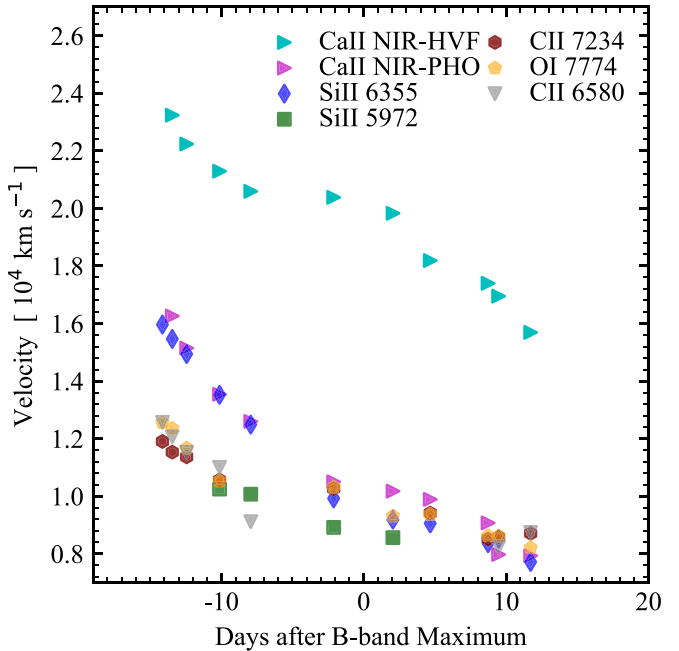
Figure 14. Velocity evolution of different elements measured from spectra of SN 2017hpa.
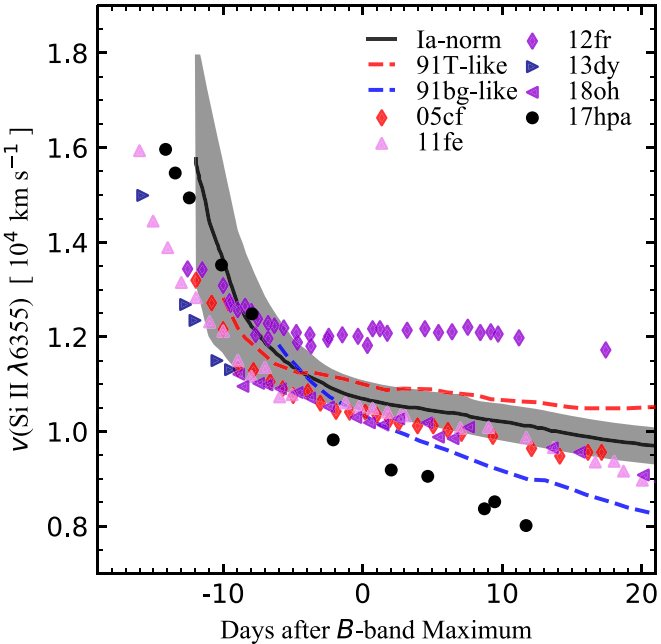
Figure 15. Velocity evolution of SN 2017hpa as derived from the absorption minimum of Si II $\lambda6355$, compared with SNe 2005cf, 2011fe, 2013dy, and 2018oh. The average velocity curves obtained for SN 1991T-like and SN 1991bg-like SNe are overplotted as red and blue dashed lines, respectively. The normal subclass of SNe Ia is plotted with a black solid line. The shaded region represents the 1σ uncertainty for the mean velocity curve of normal SNe Ia. Data for the comparison SNe and the region of normal SNe Ia are extracted from Li et al. (2019).

Table 5
Parameters of SN 2017hpa

Parameter	Value
Photometric	
B_{max}	14.88 ± 0.02 mag
$B_{\mathrm{max}} - V_{\mathrm{max}}$	0.005 ± 0.007 mag
$M_{\mathrm{max}}(B)$	-19.12 ± 0.11 mag
$E(B-V)_{\mathrm{host}}$	0.06 ± 0.06 mag
$\Delta m_{15}(B)$	1.02 ± 0.07 mag
s_{BV}	0.94 ± 0.03
$t_{\mathrm{max}}(B)$	$58,066.64 \pm 0.36$ days
t_0	$58,050.22 \pm 1.20$ days
τ_{rise}	18.26 ± 0.97 days
$L_{\mathrm{bol}}^{\mathrm{max}}$	1.25×10^{43} erg s^{-1}
$M_{^{56}\mathrm{Ni}}$	$0.63 \pm 0.02\ M_\odot$
Spectroscopic	
$v_0(\mathrm{Si\ II})$	9550 ± 170 km s^{-1}
$\dot{v}(\mathrm{Si\ II})$	130 ± 7 km s^{-1} day^{-1}
$R(\mathrm{Si\ II})$	0.18 ± 0.03

gradients (Blondin et al. 2011). However, these two scenarios are not suited to SN 2017hpa, which has a low velocity but high velocity gradient. Alternatively, the effective mixing of heavy elements in the SN ejecta may lead to the high velocity gradient of the HVG subclass, while the inefficient mixing may cause the low velocity gradient of the LVG subclass (Blondin et al. 2012; Sahu et al. 2013).

5.3. Prominent Carbon Features

Detection of unburned carbon is important for constraining the explosion mechanisms or progenitor systems of SNe Ia, and
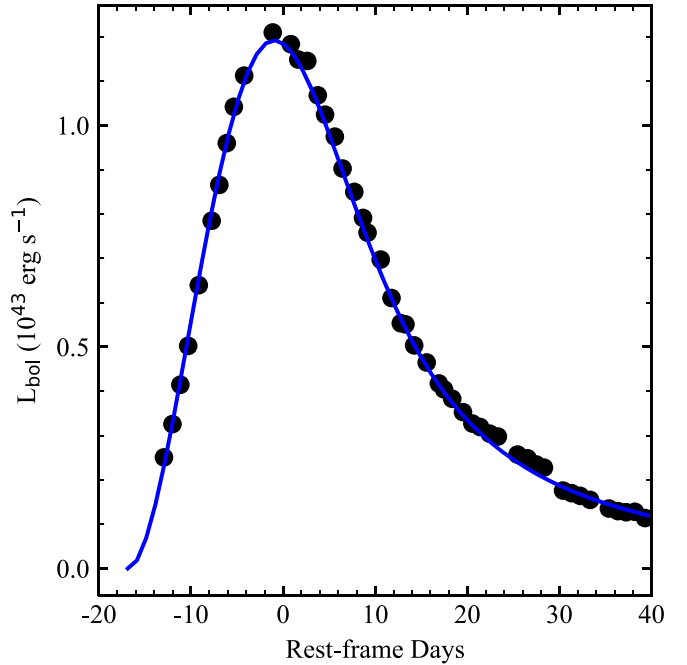
Figure 16. Quasi-bolometric light curve (dots) with an Arnett (1982) radiation diffusion model (blue curve).

different explosion models predict the presence of unburned material in different regions of the ejecta (Fink et al. 2010; Pakmor et al. 2012; Sim et al. 2012; Seitenzahl et al. 2013; Shen et al. 2018; Li et al. 2021). The velocities of IMEs in DDT will increase with the explosion strength, leading to the diffusion of unburned materials farther outward (Fink et al. 2010; Blondin et al. 2011). The carbon and oxygen have distinct velocity distributions in the delayed-detonation model, while a similar velocity distribution is predicted in the violent merger (Röpke et al. 2012). For those carbon-positive SNe Ia such as SNe 2005di, 2005el, 2005ki, and SNF20080514-002, the absorption notch due to C II $\lambda6580$ usually disappears about one week before maximum light (Thomas et al. 2011). Recent studies suggest that some SNe Ia or peculiar SNe Ia exhibit unusually persistent carbon features in their spectra, such as SN 2002fk (Cartier et al. 2014), iPTF14atg (Cao et al. 2015), and SN 2018oh (Li et al. 2019). SN 2017hpa is another example showing such a prominent C II $\lambda6580$ feature at early epochs ($t \leqslant -7.9$ days), and this carbon feature disappeared in near-maximum-light spectra. However, unlike other SNe Ia, the carbon feature seems to reemerge at phases from $t \sim +8.7$ to $\sim +11.7$ days after maximum light.

The velocity ratio of C II $\lambda6580$ to Si II $\lambda6355$ is an important parameter for setting constraints on the explosion models of SNe Ia (Parrent et al. 2011; Folatelli et al. 2012). As shown in Figure 13, the typical value of such a velocity ratio is ~ 1.05 for SNe Ia (Silverman & Filippenko 2012). However, the mean R (C II/Si II) is measured to be 0.81 for SN 2017hpa, much lower than the typical value. As noted by Silverman et al. (2012a), for a given object, the R(C II/Si II) usually increases somewhat with time. This conclusion may be also supported by the data presented by Parrent et al. (2011). Scalzo et al. (2010) suggested that the prominent C II $\lambda6580$ feature, concurrent with low velocities, could be associated with a preexplosion envelope of progenitor material originating from the merger of two white dwarfs. With the receding of the photosphere of SNe
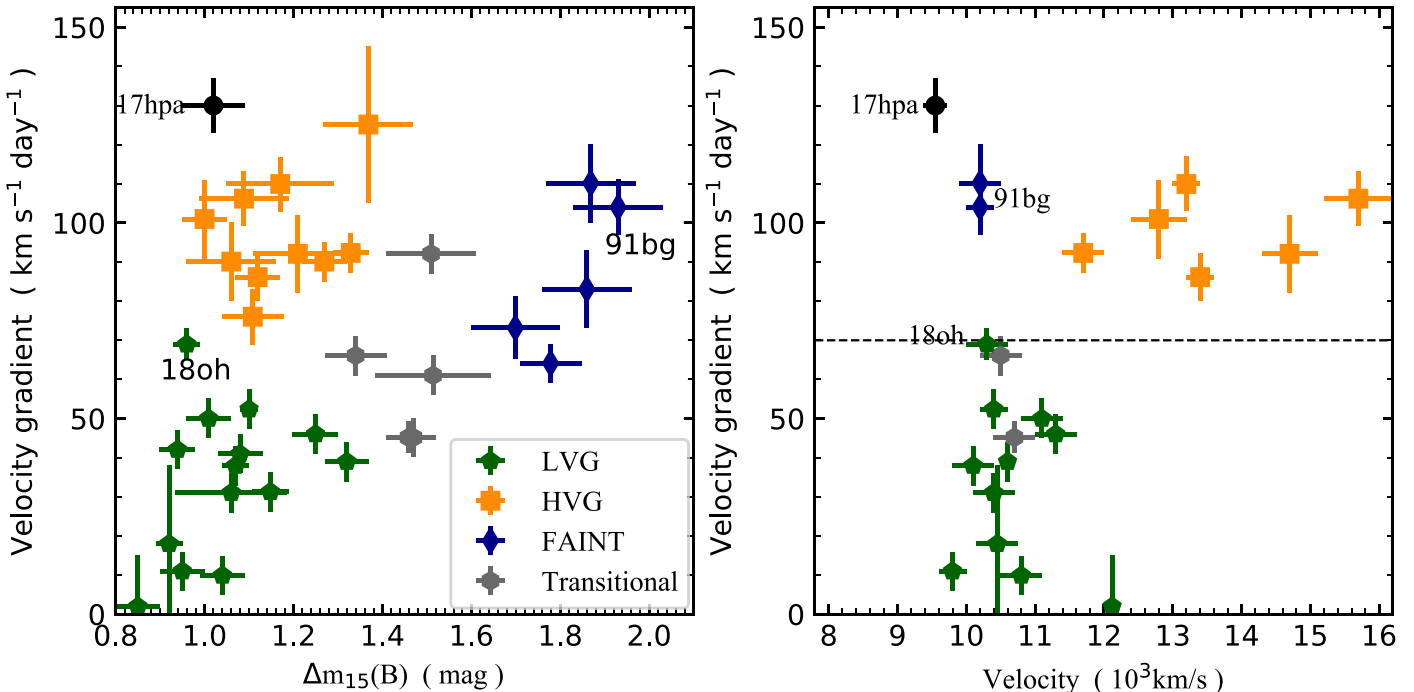
Figure 17. Spectroscopic subclassification of SN 2017hpa (as marked with black dot) based on the scheme of Benetti et al. (2005). Left panel: $\Delta m_{15}(B)$ is plotted with respect to the velocity gradient, which is measured from Si II λ6355. The SNe from different subtypes are taken from Benetti et al. (2005) and Chakradhari et al. (2018), the four transitional objects are from Pastorello et al. (2007) and Sahu et al. (2013), SN 2005cf is from Wang et al. (2009b), and SN 2018oh is from Li et al. (2019). Right panel: scatter plot of the velocity measured from Si II λ6355 near maximum light vs. the velocity gradient. The velocities are taken from Silverman et al. (2012b) and Wang et al. (2019b). The horizontal dashed line in the left panel marks the boundary between HVG and LVG, which is 70 km s^{-1} day^{-1} (Benetti et al. 2005).

Ia, the ejecta of the inner layer with a more uniform velocity distribution begin to show up, which leads to the observed phenomenon that the R(C II/Si II) increases slowly with time. The abundance distribution inferred from the violent merger model indicates that both carbon and oxygen can be mixed deep into the inner layer of the ejecta (Röpke et al. 2012). The prominent carbon features and high velocity gradient may suggest that SN 2017hpa is reminiscent of a low-luminosity subclass like SN 1991bg. However, the light curves and color curves of SN 2017hpa are quite different from those of low-luminosity objects like SN 2005bl (Taubenberger et al. 2008) or even transitional objects like SN 2004eo (Pastorello et al. 2007).

To investigate the abnormal behavior of SN 2017hpa, we perform a further comparison of C II λ6580 absorption in Figure 18, where the sample includes SNe 2002fk, 2005el, 2005cf, 2009dc, 2011fe, 2012cg, 2013dy, and 2018oh. The spectra of the comparison SNe are taken from other works (Wang et al. 2009b; Silverman et al. 2012a; Yaron & Gal-Yam 2012; Zhai et al. 2016; Zhang et al. 2016b; Guillochon et al. 2017; Li et al. 2019; Stahl et al. 2020b). In the spectra of SN 2013dy, a strong C II λ6580 absorption feature can be found with a velocity up to $\sim$16,300 km s^{-1} at early epochs, but this absorption feature quickly fades away at $t \approx -12.9$, $\sim$3 days after explosion (Zheng et al. 2013; Pan et al. 2015a). SN 2012cg shows moderately strong C II λ6580 at the same phase with respect to SN 2017hpa, and the C II absorption feature lasts until $\sim$8 days before maximum light (Silverman et al. 2012a). The spectra of SN 2009dc exhibit a very prominent C II λ6580 absorption that lasts for a long time, and this SN is proposed to result from a super-Chandrasekhar mass

progenitor system (Howell et al. 2006; Tanaka et al. 2010; Silverman et al. 2011; Taubenberger et al. 2011). SNe 2005cf, 2005el, and 2011fe show moderate C II features along their spectra evolution, while SNe 2002fk and 2018oh have C II absorption comparable to that of SN 2017hpa. All three of these normal SNe Ia show a prominent C II absorption feature. The C II absorption lines could be detected even in the spectra at $\sim$7 days after B-band maximum light.

Previous studies suggest that carbon-positive SNe Ia tend to have bluer optical or UV colors (Thomas et al. 2011; Silverman et al. 2012a; Milne et al. 2013). Swift/UVOT observations also suggest that SNe Ia with prominent carbon features are NUV-blue objects (Roming et al. 2005; Milne et al. 2010; Thomas et al. 2011). The only exception is SN 2005cf, which belongs to the NUV-red subgroup but with signatures of carbon features (Silverman et al. 2012a; Milne et al. 2013). SN 2017hpa is also an NUV-red SN Ia and has carbon in its early-time spectra. Based on model comparisons, Brown et al. (2019) suggested that the physical origins of the NUV-blue and NUV-red subclasses are likely related to metal abundance. As suggested by Heringer et al. (2017), the C II absorption features could be hidden by the emission from iron, leading to a lower metallicity within the outer layers of SNe Ia with carbon signatures. However, if metallicity is the dominant origin of the NUV differences and the presence of C II features, a continuous distribution is expected in each of them (Brown et al. 2019). A large sample of SNe Ia with positive C II features is needed to model metallicity effects on C II absorption in the spectra.

Based on the above discussions, SN 2017hpa shows prominent carbon features with a distinct evolution, a low C II λ6580-to-Si II λ6355 velocity ratio, and normal ejecta velocity but a high
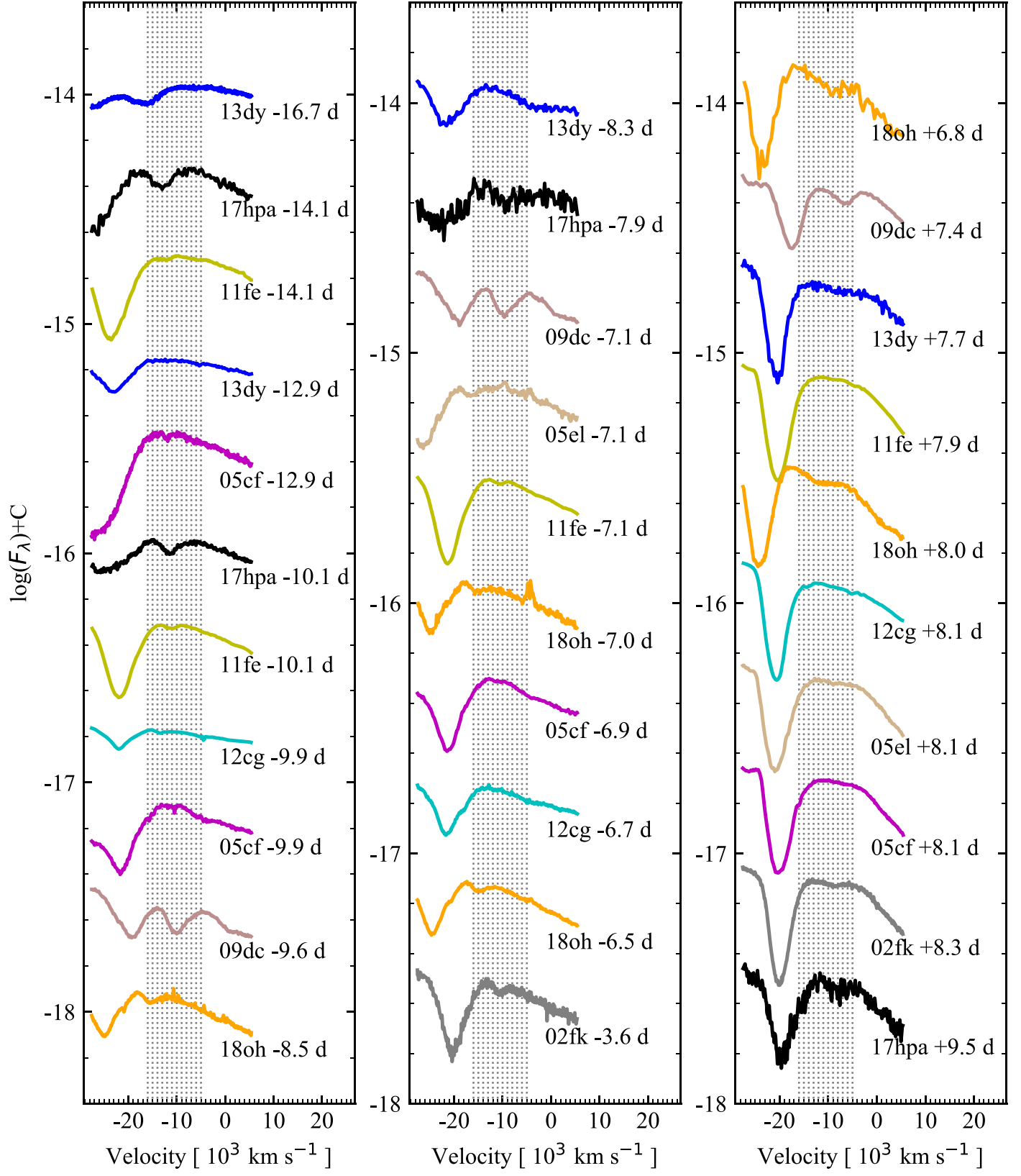
Figure 18. The C II λ6580 evolution of SN 2017hpa compared to some well-observed SNe Ia, including SNe 2002fk, 2005el, 2005cf, 2009dc, 2011fe, 2012cg, 2013dy, and 2018oh.

velocity gradient, all of which are unusual for known subtypes of normal SNe Ia. We suggest that SN 2017hpa could result from a violent merger explosion of two carbon–oxygen white dwarfs, which brings about the prominent and distinct C II features in its spectra. The deep mixing of the SN ejecta may result in the high velocity gradient of SN 2017hpa.

6. Conclusion

In this paper, we present extensive optical photometry and spectroscopy of the Type Ia SN 2017hpa, which was discovered at a relatively young phase. This object can be put into the category of normal and NUV-red SNe Ia, with $\Delta m_{15}(B) = 1.02 \pm 0.07$ mag and an absolute B-band magnitude $M_{\max}(B) = -19.12 \pm 0.11$ mag.

The quasi-bolometric light curve of SN 2017hpa is established by using extensive UV/optical photometric observations. Arnett's ^{56}Ni and ^{56}Co radioactive-decay-driven radiation diffusion model is utilized to fit the quasi-bolometric light curve, deriving a peak luminosity of SN 2017hpa as $L_{\rm peak} = 1.25 \times 10^{43}$ erg s^{-1}. The mass of nickel synthesized during the explosion is estimated to be $M_{\rm Ni} = 0.63 \pm 0.02\, M_{\odot}$, and the ejecta mass $M_{\rm ej} = 0.70 \pm 0.22\, M_{\odot}$.

The spectral evolution of SN 2017hpa is roughly the same as that of normal SNe Ia such as SN 2018oh. However, prominent C II absorption and abnormal velocity evolution distinguish it from other normal SNe Ia. The carbon and oxygen features appear stronger than in normal SNe Ia and lasted until about 10 days after maximum light, and both the carbon and oxygen have a lower velocity than intermediate-mass elements such as Si II and Ca II. Although SN 2017hpa has a typical ejecta velocity, $\sim 9550 \pm 170$ km s^{-1} as measured near the maximum light, it has an unusually large velocity gradient ($\sim 130 \pm 7$ km s^{-1} day^{-1}) in comparison with other normal SNe Ia. The significant amount of unburned C and O in the ejecta, lower velocity relative to IMEs, and large velocity gradient are more consistent with the merger model. More observations and detailed modeling are needed to reveal the exact explosion physics in objects like SN 2017hpa.

ORCID iDs

Xiangyun Zeng ● https://orcid.org/0000-0002-8049-202X
Xiaofeng Wang ● https://orcid.org/0000-0002-7334-2357
Ali Esamdin ● https://orcid.org/0000-0003-1845-4900
Craig Pellegrino ● https://orcid.org/0000-0002-7472-1279
WeiKang Zheng ● https://orcid.org/0000-0002-2636-6508
Jujia Zhang ● https://orcid.org/0000-0002-8296-2590
Wenxiong Li ● https://orcid.org/0000-0002-0096-3523
Alexei V. Filippenko ● https://orcid.org/0000-0003-3460-0103
Edward A. Baron ● https://orcid.org/0000-0001-5393-1608
Jamison Burke ● https://orcid.org/0000-0003-0035-6659
James M. DerKacy ● https://orcid.org/0000-0002-7566-6080
Curtis McCully ● https://orcid.org/0000-0001-5807-7893
Daichi Hiramatsu ● https://orcid.org/0000-0002-1125-9187
Griffin Hosseinzadeh ● https://orcid.org/0000-0002-0832-2974
Benjamin E. Stahl ● https://orcid.org/0000-0002-3169-3167
Stefano Valenti ● https://orcid.org/0000-0001-8818-0795
Danfeng Xiang ● https://orcid.org/0000-0002-1089-1519
Tianmeng Zhang ● https://orcid.org/0000-0002-8531-5161

References

Abbott, T. M. C., Allam, S., Andersen, P., et al. 2019, ApJL, 872, L30
Aldering, G., Antilogus, P., Bailey, S., et al. 2006, ApJ, 650, 510
Arnett, W. D. 1982, ApJ, 253, 785
Astropy Collaboration, Robitaille, T. P., Tollerud, E. J., et al. 2013, A&A, 558, A33
Benetti, S., Cappellaro, E., Mazzali, P. A., et al. 2005, ApJ, 623, 1011
Betoule, M., Kessler, R., Guy, J., et al. 2014, A&A, 568, A22
Blondin, S., Kasen, D., Röpke, F. K., et al. 2011, MNRAS, 417, 1280
Blondin, S., Matheson, T., Kirshner, R. P., et al. 2012, AJ, 143, 126
Bloom, J. S., Kasen, D., Shen, K. J., et al. 2012, ApJL, 744, L17
Branch, D., Dang, L. C., Hall, N., et al. 2006, PASP, 118, 560
Branch, D., Fisher, A., & Nugent, P. 1993, AJ, 106, 2383
Breeveld, A. A., Landsman, W., Holland, S. T., et al. 2011, AIPC, 1358, 373
Brown, P. J., Breeveld, A. A., Holland, S., et al. 2014, Ap&SS, 354, 89

Brown, P. J., Hosseinzadeh, G., Jha, S. W., et al. 2019, ApJ, 877, 152
Brown, T. M., Baliber, N., Bianco, F. B., et al. 2013, PASP, 125, 1031
Burns, C. R., Parent, E., Phillips, M. M., et al. 2018, ApJ, 869, 56
Burns, C. R., Stritzinger, M., Phillips, M. M., et al. 2011, AJ, 141, 19
Burns, C. R., Stritzinger, M., Phillips, M. M., et al. 2014, ApJ, 789, 32
Cao, Y., Kulkarni, S. R., Howell, D. A., et al. 2015, Natur, 521, 328
Cardelli, J. A., Clayton, G. C., & Mathis, J. S. 1989, ApJ, 345, 245
Cartier, R., Hamuy, M., Pignata, G., et al. 2014, ApJ, 789, 89
Chakradhari, N. K., Sahu, D. K., Anupama, G. C., et al. 2018, MNRAS,
    474, 2502
Chambers, K. C., Magnier, E. A., Metcalfe, N., et al. 2016, arXiv:1612.05560
Chandrasekhar, S. 1957, An Introduction to the Study of Stellar Structure
Chatzopoulos, E., Wheeler, J. C., & Vinko, J. 2012, ApJ, 746, 121
Chatzopoulos, E., Wheeler, J. C., Vinko, J., et al. 2013, ApJ, 773, 76
Chen, D., Wang, J.-C., Xu, J., et al. 2001, PYunO, 4, 42
Childress, M. J., Filippenko, A. V., Ganeshalingam, M., et al. 2014, MNRAS,
    437, 338
Ciaraldi-Schoolmann, F., Seitenzahl, I. R., & Röpke, F. K. 2013, A&A,
    559, A117
Cui, X., Wang, B., Wu, C.-Y., et al. 2020, RAA, 20, 003
Dilday, B., Howell, D. A., Cenko, S. B., et al. 2012, Sci, 337, 942
Fan, Z., Wang, H., Jiang, X., et al. 2016, PASP, 128, 115005
Filippenko, A. V. 1997, ARA&A, 35, 309
Filippenko, A. V. 2003, in From Twilight to Highlight: The Physics of
    Supernovae, ed. W. Hillebrandt & B. Leibundgut (Berlin: Springer), 171
Filippenko, A. V. 2005, in 1604–2004, Supernovae as Cosmological
    Lighthouses, ed. M. Turatto et al. (San Francisco, CA: ASP), 87
Filippenko, A. V., Li, W. D., Treffers, R. R., & Modjaz, M. 2001, in IAU
    Symp. 183, Small-Telescope Astronomy on Global Scales, ed. W. P. Chen,
    C. Lemme, & B. Paczyński (Cambridge: Cambridge Univ. Press), 121
Filippenko, A. V., Richmond, M. W., Branch, D., et al. 1992a, AJ, 104, 1543
Filippenko, A. V., Richmond, M. W., Matheson, T., et al. 1992b, ApJL,
    384, L15
Fink, M., Röpke, F. K., Hillebrandt, W., et al. 2010, A&A, 514, A53
Flewelling, H. A., Magnier, E. A., Chambers, K. C., et al. 2020, ApJS, 251, 7
Folatelli, G., Phillips, M. M., Morrell, N., et al. 2012, ApJ, 745, 74
Foley, R. J., Sanders, N. E., & Kirshner, R. P. 2011, ApJ, 742, 89
Gagliano, , Post, R., Weinberg, E., et al. 2017, Transient Name Server
    Discovery Report, 2017-1164
Ganeshalingam, M., Li, W., Filippenko, A. V., et al. 2010, ApJS, 190, 418
Garavini, G., Nobili, S., Taubenberger, S., et al. 2007, A&A, 471, 527
García-Berro, E., & Lorén-Aguilar, P. 2017, in Dynamical Mergers, ed.
    A. W. Alsabti & P. Murdin (Berlin: Springer), 1237
Gehrels, N., Chincarini, G., Giommi, P., et al. 2004, ApJ, 611, 1005
González Hernández, J. I., Ruiz-Lapuente, P., Tabernero, H. M., et al. 2012,
    Natur, 489, 533
Guevel, D., & Hosseinzadeh, G. 2017, Dguevel/Pyzogy: Initial Release,
    v0.0.1, Zenodo, doi:10.5281/zenodo.1043973
Guillochon, J., Parrent, J., Kelley, L. Z., et al. 2017, ApJ, 835, 64
Guy, J., Astier, P., Nobili, S., et al. 2005, A&A, 443, 781
Hamuy, M., Phillips, M. M., Suntzeff, N. B., et al. 2003, Natur, 424, 651
Henden, A. A., Templeton, M., Terrell, D., et al. 2016, VizieR Online Data
    Catalog, II/336
Heringer, E., van Kerkwijk, M. H., Sim, S. A., et al. 2017, ApJ, 846, 15
Höflich, P., Hsiao, E. Y., Ashall, C., et al. 2017, ApJ, 846, 58
Hosseinzadeh, G., Sand, D. J., Valenti, S., et al. 2017, ApJL, 845, L11
Howell, D. A. 2011, NatCo, 2, 350
Howell, D. A., Sullivan, M., Nugent, P. E., et al. 2006, Natur, 443, 308
Hsiao, E. Y., Marion, G. H., Phillips, M. M., et al. 2013, ApJ, 766, 72
Huang, F., Li, J.-Z., Wang, X.-F., et al. 2012, RAA, 12, 1585
Hunter, J. D. 2007, CSE, 9, 90
Iben, I., & Tutukov, A. V. 1984, ApJS, 54, 335
Jiang, X., Xu, D., & Hu, J. 1999, AcApS, 19, 220
Kasen, D. 2010, ApJ, 708, 1025
Khokhlov, A. M. 1991, A&A, 245, 114
Kromer, M., Sim, S. A., Fink, M., et al. 2010, ApJ, 719, 1067
Landolt, A. U. 1992, AJ, 104, 340
Leibundgut, B., Kirshner, R. P., Phillips, M. M., et al. 1993, AJ, 105, 301
Leloudas, G., Stritzinger, M. D., Sollerman, J., et al. 2009, A&A, 505, 265
Li, W., Filippenko, A. V., Chornock, R., et al. 2003, PASP, 115, 844
Li, W., Filippenko, A. V., & Riess, A. G. 2001, ApJ, 546, 719
Li, W., Wang, X., Bulla, M., et al. 2021, ApJ, 906, 99
Li, W. X., Wang, X., Vinkó, J., et al. 2019, ApJ, 870, 12
Livne, E. 1990, ApJL, 354, L53
Maeda, K., Benetti, S., Stritzinger, M., et al. 2010, Natur, 466, 82
Magnier, E. A., Schlafly, E. F., Finkbeiner, D. P., et al. 2020, ApJ, 251, 6

Maguire, K., Sullivan, M., Ellis, R. S., et al. 2012, MNRAS, 426, 2359
Maguire, K., Sullivan, M., Pan, Y.-C., et al. 2014, MNRAS, 444, 3258
Maguire, K., Sullivan, M., Patat, F., et al. 2013, MNRAS, 436, 222
Mandel, K. S., Foley, R. J., & Kirshner, R. P. 2014, ApJ, 797, 75
Maoz, D., Mannucci, F., & Nelemans, G. 2014, ARA&A, 52, 107
Mazzali, P. A., Ashall, C., Pian, E., et al. 2018, MNRAS, 476, 2905
Mazzali, P. A., Sullivan, M., Hachinger, S., et al. 2014, MNRAS, 439, 1959
Miller, J. S., & Stone, R. P. S. 1993, Lick Observatory Technical Report, 66
Milne, P. A., Brown, P. J., Roming, P. W. A., et al. 2010, ApJ, 721, 1627
Milne, P. A., Brown, P. J., Roming, P. W. A., et al. 2013, ApJ, 779, 23
Munari, U., Henden, A., Belligoli, R., et al. 2013, NewA, 20, 30
Nomoto, K. 1982, ApJ, 253, 798
Nomoto, K., Iwamoto, K., & Kishimoto, N. 1997, Sci, 276, 1378
Nugent, P., Phillips, M., Baron, E., et al. 1995, ApJL, 455, L147
Olling, R. P., Mushotzky, R., Shaya, E. J., et al. 2015, Natur, 521, 332
Pakmor, R., Kromer, M., Taubenberger, S., et al. 2012, ApJL, 747, L10
Pan, Y.-C., Foley, R. J., Kromer, M., et al. 2015a, MNRAS, 452, 4307
Pan, Y.-C., Sullivan, M., Maguire, K., et al. 2015b, MNRAS, 446, 354
Parrent, J. T., Thomas, R. C., Fesen, R. A., et al. 2011, ApJ, 732, 30
Pastorello, A., Mazzali, P. A., Pignata, G., et al. 2007, MNRAS, 377, 1531
Patat, F., Chandra, P., Chevalier, R., et al. 2007, Sci, 317, 924
Perlmutter, S., Aldering, G., Goldhaber, G., et al. 1999, ApJ, 517, 565
Phillips, M. M. 1993, ApJL, 413, L105
Phillips, M. M., Lira, P., Suntzeff, N. B., et al. 1999, AJ, 118, 1766
Phillips, M. M., Wells, L. A., Suntzeff, N. B., et al. 1992, AJ, 103, 1632
Piersanti, L., Tornambé, A., & Castellani, V. 2004, MNRAS, 353, 243
Piro, A. L., & Morozova, V. S. 2016, ApJ, 826, 96
Piro, A. L., & Nakar, E. 2013, ApJ, 769, 67
Plewa, T., Calder, A. C., & Lamb, D. Q. 2004, ApJL, 612, L37
Raskin, C., & Kasen, D. 2013, ApJ, 772, 1
Riess, A. G., Casertano, S., Yuan, W., et al. 2018, ApJ, 855, 136
Riess, A. G., Filippenko, A. V., Challis, P., et al. 1998, AJ, 116, 1009
Riess, A. G., Filippenko, A. V., Li, W., et al. 1999, AJ, 118, 2675
Riess, A. G., Press, W. H., & Kirshner, R. P. 1996, ApJ, 473, 88
Rogers, R. A. P. 1920, Natur, 105, 138
Roming, P. W. A., Kennedy, T. E., Mason, K. O., et al. 2005, SSRv, 120, 95
Röpke, F. K., Kromer, M., Seitenzahl, I. R., et al. 2012, ApJL, 750, L19
Ruiz-Lapuente, P., Cappellaro, E., Turatto, M., et al. 1992, ApJL, 387, L33
Sahu, D. K., Anupama, G. C., & Anto, P. 2013, MNRAS, 430, 869
Scalzo, R. A., Aldering, G., Antilogus, P., et al. 2010, ApJ, 713, 1073
Scalzo, R. A., Parent, E., Burns, C., et al. 2019, MNRAS, 483, 628
Schaefer, B. E., & Pagnotta, A. 2012, Natur, 481, 164
Schlafly, E. F., & Finkbeiner, D. P. 2011, ApJ, 737, 103
Schlegel, D. J., Finkbeiner, D. P., & Davis, M. 1998, ApJ, 500, 525
Seitenzahl, I. R., Ciaraldi-Schoolmann, F., Röpke, F. K., et al. 2013, MNRAS,
    429, 1156
Shen, K. J., Guillochon, J., & Foley, R. J. 2013, ApJL, 770, L35
Shen, K. J., Kasen, D., Miles, B. J., et al. 2018, ApJ, 854, 52
Shen, K. J., & Moore, K. 2014, ApJ, 797, 46
Shporer, A., Brown, T., Lister, T., et al. 2011, IAU Symp. 276, The
    Astrophysics of Planetary Systems: Formation, Structure, and Dynamical
    Evolution (Cambridge: Cambridge Univ. Press), 553
Silverman, J. M., & Filippenko, A. V. 2012, MNRAS, 425, 1917
Silverman, J. M., Foley, R. J., Filippenko, A. V., et al. 2012a, MNRAS,
    425, 1789
Silverman, J. M., Ganeshalingam, M., Li, W., et al. 2011, MNRAS, 410, 585
Silverman, J. M., Kong, J. J., & Filippenko, A. V. 2012b, MNRAS, 425, 1819
Silverman, J. M., Nugent, P. E., Gal-Yam, A., et al. 2013, ApJS, 207, 3
Silverman, J. M., Vinkó, J., Marion, G. H., et al. 2015, MNRAS, 451, 1973
Sim, S. A., Fink, M., Kromer, M., et al. 2012, MNRAS, 420, 3003
Springob, C. M., Haynes, M. P., Giovanelli, R., et al. 2005, ApJS, 160, 149
Stahl, B. E., Martínez-Palomera, J., Zheng, W., et al. 2020a, MNRAS,
    496, 3553
Stahl, B. E., Zheng, W., de Jaeger, T., et al. 2019, MNRAS, 490, 3882
Stahl, B. E., Zheng, W., de Jaeger, T., et al. 2020b, MNRAS, 492, 4325
Stanishev, V., Goobar, A., Benetti, S., et al. 2007, A&A, 469, 645
Sternberg, A., Gal-Yam, A., Simon, J. D., et al. 2011, Sci, 333, 856
Stetson, P. B. 1987, PASP, 99, 191
Su, D. Q., Zhou, B. F., & Yu, X. M. 1989, ScChA, 11, 1187
Syam, M. I. 2003, JApSc, 3, 9
Tanaka, M., Kawabata, K. S., Yamanaka, M., et al. 2010, ApJ, 714, 1209
Tanikawa, A., Nomoto, K., Nakasato, N., et al. 2019, ApJ, 885, 103
Taubenberger, S., Benetti, S., Childress, M., et al. 2011, MNRAS, 412, 2735
Taubenberger, S., Hachinger, S., Pignata, G., et al. 2008, MNRAS, 385, 75
Taubenberger, S., Benetti, S., Tomasella, L., et al. 2017, Transient Name
    Server Classification Report, 2017-1173

Thomas, R. C., Aldering, G., Antilogus, P., et al. 2011, ApJ, 743, 27
Thompson, T. A. 2011, ApJ, 741, 82
Tody, D. 1986, Proc. SPIE, 627, 733
Tody, D. 1993, adass II, 52, 173
Tucker, M. A., Shappee, B. J., & Wisniewski, J. P. 2019, ApJL, 872, L22
Valenti, S., Howell, D. A., Stritzinger, M. D., et al. 2016, MNRAS, 459, 3939
Wang, C.-J., Bai, J.-M., Fan, Y.-F., et al. 2019a, RAA, 19, 149
Wang, L., & Hu, J. 1994, Natur, 369, 380
Wang, X., Chen, J., Wang, L., et al. 2019b, ApJ, 882, 120
Wang, X., Filippenko, A. V., Ganeshalingam, M., et al. 2009a, ApJL, 699, L139
Wang, X., Li, W., Filippenko, A. V., et al. 2008, ApJ, 675, 626
Wang, X., Li, W., Filippenko, A. V., et al. 2009b, ApJ, 697, 380
Wang, X., Wang, L., Filippenko, A. V., et al. 2013, Sci, 340, 170
Wang, X., Wang, L., Pain, R., et al. 2006, ApJ, 645, 488
Wang, X., Wang, L., Zhou, X., et al. 2005, ApJL, 620, L87
Waters, C. Z., Magnier, E. A., Price, P. A., et al. 2020, ApJS, 251, 4

Webbink, R. F. 1984, ApJ, 277, 355
Whelan, J., & Iben, I. 1973, ApJ, 186, 1007
Willick, J. A., Courteau, S., Faber, S. M., et al. 1997, ApJS, 109, 333
Woosley, S. E., Kerstein, A. R., Sankaran, V., et al. 2009, ApJ, 704, 255
Woosley, S. E., Taam, R. E., & Weaver, T. A. 1986, ApJ, 301, 601
Yamanaka, M., Kawabata, K. S., Kinugasa, K., et al. 2009, ApJL, 707, L118
Yaron, O., & Gal-Yam, A. 2012, PASP, 124, 668
Zackay, B., Ofek, E. O., & Gal-Yam, A. 2016, ApJ, 830, 27
Zhai, Q., Zhang, J.-J., Wang, X.-F., et al. 2016, AJ, 151, 125
Zhang, J.-C., Fan, Z., Yan, J.-Z., et al. 2016a, PASP, 128, 105004
Zhang, J.-C., Ge, L., Lu, X.-M., et al. 2015, PASP, 127, 1292
Zhang, K., Wang, X., Zhang, J., et al. 2016b, ApJ, 820, 67
Zhao, X., Maeda, K., Wang, X., et al. 2016, ApJ, 826, 211
Zhao, X., Wang, X., Maeda, K., et al. 2015, ApJS, 220, 20
Zheng, W., & Filippenko, A. V. 2017, ApJL, 838, L4
Zheng, W., Filippenko, A. V., Mauerhan, J., et al. 2017, ApJ, 841, 64
Zheng, W., Silverman, J. M., Filippenko, A. V., et al. 2013, ApJL, 778, L15